Micromechanics reveal strain rate dependent transition between dislocation mechanisms in a dual phase high entropy alloy

Szilvia Kalácska, Amit Sharma, Rajaprakash Ramachandramoorthy, Ádám
Vida, Florian Tropper, Renato Pero, Damian Frey, Xavier Maeder, Johann
Michler, Péter Dusán Ispánovity, et al.

Micromechanics reveal strain rate dependent transition between dislocation mechanisms in a dual phase high entropy alloy

Szilvia Kalácska[a,b,*], Amit Sharma[b], Rajaprakash Ramachandramoorthy[b,c], Ádám Vida[d], Florian Tropper[e], Renato Pero[e], Damian Frey[e], Xavier Maeder[b], Johann Michler[b], Péter Dusán Ispánovity[f], Guillaume Kermouche[a]

[a]*Mines Saint-Etienne, Univ Lyon, CNRS, UMR 5307 LGF, Centre SMS, 158 cours Fauriel 42023 Saint-Étienne, France*
[b]*Empa, Swiss Federal Laboratories for Materials Science and Technology, Laboratory of Mechanics of Materials and Nanostructures, CH-3602 Thun, Feuerwerkerstrasse 39. Switzerland*
[c]*Max-Planck-Institute für Eisenforschung, Max Planck Strasse 1, 40472 Düsseldorf, Germany*
[d]*Bay Zoltán Nonprofit Ltd. for Applied Research, Kondorfa u.1., H-1116 Budapest, Hungary*
[e]*Alemnis AG, Business Park Gwatt, Schorenstrasse 39, 3645 Gwatt (Thun), Switzerland*
[f]*ELTE Eötvös Loránd University, Department of Materials Physics, Pázmány Péter sétany 1/a, 1117 Budapest, Hungary*

Abstract

An equimolar NiCoFeCrGa high entropy alloy having dual-phase homogeneous components was studied, where the constituent phases exhibit distinct mechanical properties. Micropillars with various diameters were created from two differently heat treated samples, then they were compressed at slow strain rates, that revealed the material's limited sensitivity to size. On the other hand, increased strain rate sensitivity at high deformation speeds was observed, that differs substantially depending on the phase composition of the specimen. Dislocations within the two phases were studied by high resolution transmission electron microscopy and high angular resolution electron backscatter diffraction. The performed chemical analysis confirmed that slow cooling during casting create Cr-rich precipitates, that have significant impact on the global strength of the material.

Keywords: High entropy alloy, micromechanics, multiphase, microstructure, mechanical properties

1. Introduction

High entropy alloys (HEAs) are multi-principal element intermetallic alloys with at least four constituents with a crystalline structure that lacks long-range ordering. Since their first syntheses [1, 2], they have created significant interest within the materials science community due to their outstanding properties. First and foremost, they provide an exceptional trade-off in terms of high strength coupled with considerable ductility [3, 4], but they also exhibit remarkable chemical (such as enhanced corrosion resistance) and thermal properties [5, 6] as well as high irradiation resistance [7]. In addition, due to the large number of constituent elements, the tunability of HEA materials is particularly high [8, 9].

As a reult of the large number of elements, their mixing entropy is high, therefore HEAs are mostly created as thermally stable single-phase solid solutions. Still, some HEAs are different in this sense and can exhibit multiple phases in equilibrium [10, 11], that is now making several ways toward *property* and *phase engineering* [12, 13]. Alloys mainly composed of refractory elements usually have a BCC structure and exhibit high thermal stability and hardness, but are often rather brittle [14]. On the other hand, HEAs containing mostly $3d$ transition metals in near-equiatomic concentrations usually form an FCC structure, with reduced strength but high ductilty [10]. In addition, these materials often show serrated flow, that is the sudden and unpredictable drops appearing on the stress-strain curves of random size [15]. The combination of two phases in one material may allow one to achieve the best strength-ductility synergy, this is exactly the objective of the present research.

In this paper we focus on a four-component steel-like equimolar NiCoFeCr alloy doped with an *sp* element (Ga) to make a NiCoFeCrGa HEA. In the literature, the fifth component is most often Al and Cu, but more specialised elements such as Sn, B, Ga, *etc.* also occur [10, 16]. The speciality of these systems is that while the parent alloy (i.e., the 4-component NiCoFeCr) consists of pure FCC phase with good thermal stability, the doped systems are mostly dual-phase mixtures of FCC and BCC structures. The NiCoFeCrGa system [17, 18, 19, 20, 21] can be tailored on a wide scale from the cast FCC/BCC state either in terms of phase ratios or the appearance of new phases. Considering the phase transitions of the material and the fact that the ferro-paramagnetic transition takes place in a range close to room temperature in this HEA, the alloy is a good candidate for functional applications, either as a micromechanical component or as a magneto-

---

*Corresponding author
    Email address: `szilvia.kalacska@cnrs.fr` (Szilvia Kalácska)

caloric micromaterial. These applications require the understanding of mechanical properties at the micron scale. In addition, we consider this HEA as a model material for dual-phase FCC/BCC alloys, and to understand its bulk plasticity, one should investigate the mechanical properties of the distinct phases. Since the characteristic scale of the phase structure is $\sim 10\,\mu m$, experimental approaches call for tests performed at small scales with high lateral and temporal resolution. *In situ* high strain rate (HSR) testing has only been established very recently at the relevant scale [22]. Some industrial examples of HSR experimentation include the *(i)* impact resistance of turbine blades, *(ii)* studying the survival of components/devices when dropped, *(iii)* crash testing, *(iv)* metalworking operations, *etc.* Such extreme applications require clear understanding of the rate-dependent deformation kinetics. Furthermore, providing repeatable experimental data in the HSR regime can improve existing numerical models, that cannot simulate materials properties close to the quasi-static deformation regime (i.e. molecular dynamics [23]). Additionally, by looking at a combined FCC/BCC system where the compositions of the constituent phases are as close as possible, the role of the lattice structure played in the deformation dynamics can be studied.

The local mechanical behaviour of single phase HEAs have been tested rigorously at quasi-static strain rates (QSSR, $0.0001/s - 0.1/s$) [24] at room temperature by micropillar compression [25], tensile testing [26] and nanoparticle compression [27]. High strain rates (HSR, $>10/s$) have only been accessible so far at the macro-scale (mm), and by various simulation methods. The effect of irradiation [28], size effects related to lamellar orientation [29], pure FCC [30, 31], BCC [32] and HCP [33] single crystal HEAs were also experimentally investigated by micropillar compression and nanoindentation [34] at QSSR.

The comparison between single and multiple phase materials is quite difficult, not to mention the various heat treatments, alloy compositions and microstructures. Regarding the size effects, Zou *et al.* [35] reported increased yield strength at 5% deformation with decreasing pillar sizes in refractory HEA thin films. In this case, the thin film layer has a strong texture and a columnar microstructure due to the deposition process. The hardening rate was also size dependent, as smaller pillars exhibited increased hardening at higher strains. The size effect was investigated in case of pillar diameters below 1 μm, where FIB machining can play an important role, leaving a significant ion-modified layer on the surface of the specimen. However, the HEA in the current study is different from nanocrystalline and other pure single crystalline alloys.

Bulk HEA was also used to fabricate pillars with different orientations [32], and it was found that the yield stresses of micropillars are significantly larger than in case of bulk specimens. It is important to note that the studied alloy in Ref. [32] was homogenized for 7 days at a high temperature, therefore it is considered as a stabilized BCC alloy with relatively large (> 100 μm) grains. It was also

stated that this size related effect is much smaller than in case of pure metals. Size effect is usually considered as a consequence of the stochastic presence of dislocation sources in pure metals. However, yielding in HEAs is dominated by single dislocation dynamics because of the high lattice friction. Models/simulations predicting the yield stress usually only consider the jerky motion of a single dislocation[36, 37]. Therefore, in this case, collective dislocation effects do not seem to play an important role. In traditional metals, the interaction between dislocations are significant, and that determines the yield stress (e.g., Taylor hardening).

Mechanical properties not only depend on the chemical composition of the alloy but also the local non-random distributions of the constituting elements [38, 39]. Local chemical heterogeneity can be triggered by, i.e., the speed of the cooling of the samples after alloying [21]. Individually probing each phase in these complex materials require microscale experiments to be performed, which is often done by microindentation mapping on the bulk sample's surface [40, 41].

Experiments have already proved the efficiency of micron sized sample deformation (micropillar compression, tensile bar testing, microcantilever bending etc.), when a small fraction of the bulk volume can be shaped by focused ion beam (FIB) milling. The sensitivity to strain rate in case of various HEAs has been studied at mainly by indentation [42] and bulk mechanical testing [43, 44, 45, 46], occasionally by micropillar compression [47]. However, to our knowledge, strain rate sensitivity (SRS) has not yet been investigated at the HSR regime on a dual-phase HEA, therefore the SRS-behaviour of such complex materials is unknown.

The aim of the current study is to understand how a dual-phase system with two distinctive deformation behaviours may affect the global plastic response by characterizing SRS in the constituent phases. Dislocation interactions with phase and precipitation boundaries were also examined by state-of-the-art analytical methods. In this study we investigate size effects, strain rate effects and the phase related mechanical behaviour of a dual phase HEA by micropillar compression. More than a hundred micropillars with three different diameters were prepared and tested during the campaign. Furthermore, it is important to understand how micromechanical results can be influenced by the mixture of phases within a single micropillar under extreme conditions, hence, we aim to widen the applicability of micromechanical testing by performing compression tests in the ultra-high (up to $\sim 10^4/s$) strain rate regime.

2. Experimental

2.1. Sample preparation

Casting, microstructure characterization. Sample preparation was identical as reported by Vida *et*

al. [21], where the basic microstructure characterization methods were performed on these materials. For the current study, two different heat treatments were employed. *Sample 1 – S1* was heated to $T_{S1} = 1000°C$ for 1 hour and quickly cooled by water, while *Sample 2 – S2* was slowly cooled by the furnace ($T_{S2,I} = 850°C$ for 1 hour then at $T_{S2,II} = 500°C$ for 3 hours). Due to the slower cooling rate, S2 exhibited precipitates (with average diameters of $\bar{d}_{\mathrm{prec}} \sim 100 - 150$ nm) within the BCC phase, while the composition of the FCC phase remained homogeneous. In the S1 specimen, the rapid cooling did not allow the system to form nanoprecipitates in either of the constituting phases. The microstructure remained complex (dendritic FCC surrounded by BCC matrix) due to the absence of the homogenization heat treatment after casting, that forced the experimental characterization to approach the sub–5 μm scale, making micromechanics indispensable to separate the influence of phases on the global mechanical response to deformation. Orientation and phase mapping are provided in the Suppl. Material.

It is crucial to understand the subtle chemical changes between different samples and composing elements, as phase boundaries and precipitates can have major effects on the mechanical response to external load due to the modified dislocation behaviour. In Figure 1a, chemical analysis performed by time-of-flight secondary ion mass
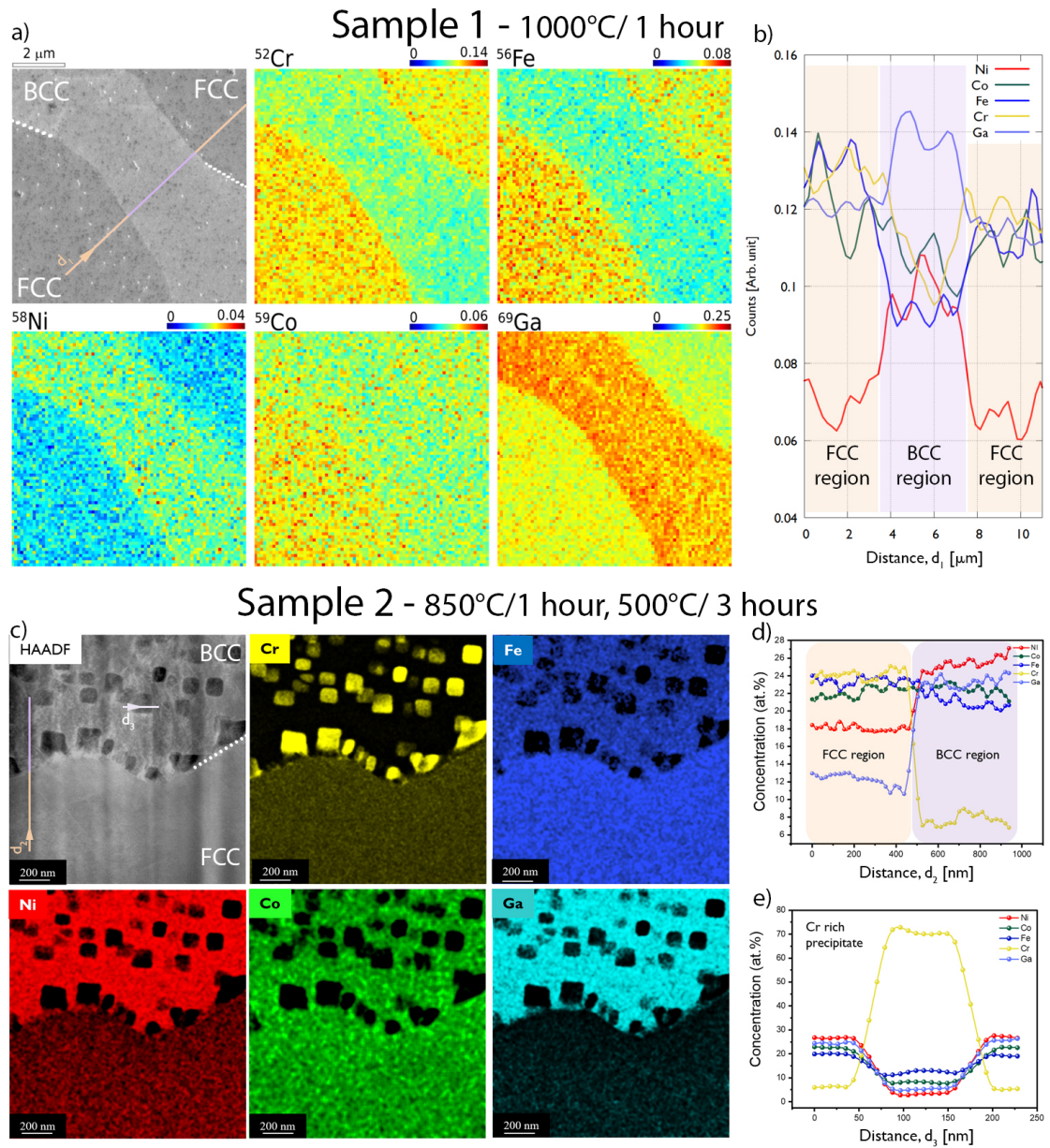
Figure 1: **Chemical composition of the samples.** Phase boundaries are indicated by white dotted lines. **(a)** Sample 1 by TOF-SIMS (color scales are in arbitrary units: counts/TOF extraction). **(b)** Chemical profile (d_1) extracted from the line marked on the secondary electron inset. **(c)** Sample 2 by TEM-EDS. Chemical profiles over the **(d)** FCC/BCC (d_2), and **(e)** BCC/precipitate regions (d_3) extracted from the line marked on the high-angle annular dark field (HAADF) panel.

3

spectroscopy (TOF-SIMS) is shown. FIB-based TOF-SIMS measurements were conducted using a TOFWERK Ag. (Switzerland) detector at 30 kV 40 pA, with additional fluorine gas injected during the sputtering process to enhance secondary ion signals. In case of S1, ^{59}Co maps show no substantial difference between FCC and BCC regions, while in cases of ^{52}Cr, ^{56}Fe, ^{58}Ni and ^{69}Ga, TOF-SIMS detected a variance in concentration between the two phases. S1 has a more homogeneously distributed composition, where precipitates cannot form due to faster cooling following casting. FCC regions seem to have somewhat higher ^{52}Cr and ^{56}Fe content, while depleted of ^{58}Ni and ^{59}Ga ions.

In order to investigate the chemical composition of S2 in more detail, transmission electron microscopy (TEM)-based energy dispersive spectroscopy (EDS) was applied (Figure 1c). It can be seen that the small cubical precipitates in S2 are rich in Cr. As they form only in the BCC phase, the matrix itself has lower ^{52}Cr content than the FCC grains [21]. It can also be observed that precipitates often prefer to accumulate along grain/phase boundaries (see also in Suppl. Fig. S14, measured by TOF-SIMS in S2 along a BCC grain boundary). The FCC phase is somewhat richer in Fe, while the BCC matrix has higher concentration of Ni and Ga, which is in good agreement with the TOF-SIMS results. In typical metal-alloy compositions, Ni and Cr play a role of γ- and α-phase stabilizing elements, however, in this HEA, the addition of Ga is the reason why the system becomes duplex [18], hence the compositional roles are different for these two elements. Concentration profiles along certain significant lines are plotted in Fig. 1b,d,e for comparison.

Before FIB preparation, the surface of the specimens was grounded and polished with diamond suspension (final step of 1 μm particle size) and with colloidal silica (Struers OP-S and OP-U). The average grain sizes of S1 and S2 are listed in Suppl. Table S1, determined by large area electron backscatter diffraction (EBSD) mapping. It is important to note that due to the expanding nature of dendritic grain growth, the statistical analysis of grain sizes (i.e., equivalent circle diameter) might be influenced by the mapping area.

FIB milling. For the micromechanical tests, circular pillars with various diameters ($\sim 1.5 - 3.5$ μm, for more detailed information, see Supplementary Material Section S6) were fabricated by FIB. These sizes made it possible to fabricate numerous pillars from one grain, and also they were chosen such that studying size related effects in both constituting phases was possible. Pillar fabrication was carried out using Tescan (Lyra3) and FEI (Helios 600i) dual beam scanning electon microscopes (SEM) through a sequence of standard beam settings (30 kV, $10 - 0.04$ nA). Images taken during the various preparation steps of a 3 μm diameter pillar are shown in Suppl. Fig. S1.

During pillar preparation, the observation was made that BCC phase sputters much faster (by a factor of 2) than FCC. This effect is shown in Suppl. Fig. S9. Due to this, micropillar bases might not necessary align with the surface of the sample, making it difficult to estimate the exact height of each pillar. As it is shown in the *Results* section (Sec. 3), sometimes micropillars had a phase boundary within the deformed volume. This was inevitable, as phase mapping could only be performed on the surface of the bulk sample. In order to ensure that the prepared pillars would contain mostly one phase, numerous micropillars were prepared. Due to the significant differences between the FCC/BCC mechanical behaviour, distinguishing pure and mixed modes is relatively straightforward after analysing the mechanical data. Furthermore, several pillars were lifted out and their cross-sections were analyzed by TEM and high (angular) resolution EBSD (HR-EBSD) mapping. This also presented a unique opportunity to investigate dislocation interactions along the phase boundaries and in the presence of precipitations.

2.2. Micromechanical testing

Micropillar compression tests provide close to ideal uniaxial conditions during deformation, leading to uniform stress/strain fields, hence this technique is favoured here as opposed to nanoindentation. Pillar compression tests were carried out using a SEM-compatible microdeformation stage (ASA, Alemnis AG). Imaging during testing was performed with a Zeiss Supra 55VP and a Zeiss DSM 962 SEM. For quasi-static studies (SR ≤ 0.1/s) strain gage based load cells (standard and mini load cell – SLC and MLC) were used to record the force acting on the micropillars and during indentation mapping [48]. HSR compression tests were performed using a piezo-based platform (SmarTip [49, 48] and Enhanced SmarTip with extended actuation distance). High fidelity data were captured using the supported hardware and software with sampling rates of 40 Hz – 1 MHz. An automatic approach with 0.15 mN threshold was applied to precisely detect the contact of the tip with each pillar. After the automatic surface detection, linear loading profiles were applied on the micropillars with varying strain rates (SR). Occasionally, when the maximum programmed displacement was reached, the tip was moved backwards by 10 nm and the displacement was kept constant for 20 s (used for the thermal drift corrections). In some cases, strain rate jump tests (SRJT) [50] were performed in order to investigate SR sensitivity using the same pillar. In these tests, an initial loading with 0.001/s was followed by 0.1/s, 0.001/s, 0.01/s and 0.001/s loading segments (see in Suppl. Fig. S10). Auto-approach procedures were not performed directly on the pillars tested at HSR due to the increase in load noise (~ 0.3 mN). In order to reduce unwanted resonance of the diamond flat punch due to high levels of acceleration/deceleration, a "proportional" displacement profile was also applied in some cases of HSR experiments (Suppl. Fig. S11, and Suppl. Table S3 marked with "prop"). In every other instances, a linear loading profile with a given tip velocity was applied (Suppl. Tables S2, S3 and S4).

Load-displacement curves of micropillars and nanoindentations were compliance corrected and analyzed by the Alemnis AMMDA v2.01 software. For the Young's modulus and hardness calculations, the unloading part of the load-displacement curves were used, along with $\bar{\nu} = 0.31$ Poisson's ratio. More information about the calculation of $\bar{\nu}$ can be found in Suppl. Section S3. FCC and mixed phase pillars usually showed a smooth elastic loading part followed by a jerky plastic part having significant stress drops characteristic to the presence of the FCC phase. In these examples, the maximum stress at the end of the elastic part (before the first main stress drop) was defined as the yield stress (σ_y). During high strain rate (HSR) testing, due to the high acceleration of the tip (reaching up to some tens of mm/s actuation velocity), an oscillating noise appears in the signal ("ringing effect"). In order to determine σ_y in such cases, the elastic and plastic parts of the stress-strain curves were fitted using a linear function, and their intersection was used to obtain the apparent yield stress values [51]. To make the evaluation consistent at all applied strain rates, σ_y values were obtained using the same yield criterion in case of low strain rate (LSR) pillar testing too, where the transition between the elastic and plastic part of the curve was smooth.

2.3. Analytical Methods

EBSD maps (Oxford Instruments Nordlys Nano and Symmetry 2) were recorded prior to and after pillar fabrication to choose grains with similar orientation. All pillars were oriented to single slip (pillar orientation and phase maps can be found in Suppl. Figs. S2–S4), depending on the available grains. Grain statistics were collected using AZtecCrystal v2.2.

HR-ESBD evaluation was performed using BLGVantage CrossCourt Rapide v4.6 software. The cross-sections of lifted out micropillars were prepared using a 30 kV 0.6 nA Ga$^+$ beam, then diffraction patterns were recorded with a 20 kV, 7 nA electron beam and an image frame averaging of 5. Some pillars were prepared for TEM analysis (see Suppl. Tables S2, S3 and S4) that were later studied by high resolution transmission Kikuchi diffraction (HR-TKD) using a 30 kV electron beam for geometrically necessary dislocation (GND) density imaging. During the evaluation, the following elastic constant coefficients were used [determined for a ferromagnetic material, in GPa] for BCC: $C_{11}^{\mathrm{BCC}} = 215.1$, $C_{12}^{\mathrm{BCC}} = 162.7$, $C_{44}^{\mathrm{BCC}} = 122.3$, and for FCC: $C_{11}^{\mathrm{FCC}} = 184.7$, $C_{12}^{\mathrm{FCC}} = 146.9$, $C_{44}^{\mathrm{FCC}} = 123.3$ [52].

Chemical analysis of the two samples were carried out using TOF-SIMS (TOFWERK AG). This technique uses the FIB beam to sputter away locally the sample [53, 54], while the detector collects and categorises the sputtered ions based on their mass. The method was chosen instead of conventional SEM-based energy dispersive spectroscopy (EDS) due to its excellent spatial (lateral and depth) resolution, as sputtered ions originate only from a top few atomic layers on the surface. It is important to note that chemical composition and crystallographic orientation influences the sputtering speed, and in case of a multiphase alloy, it would mean that the sputtered crater depth varies in the FCC/BCC regions [55]. Maps were recorded in "+" mode, using a 30 kV, 40-160 pA ion beam with fluorine inert gas injected through a gas injection system (GIS, Orsay Physics). Fluorine was applied to increase ionization probability and enhance secondary ion signals during the analysis [56]. 10-20 frames were recorded over areas of 5-10 μm, with a dwell time of 32 μs and 2×2 binning.

STEM, high-angle annular dark field (HAADF) images and selected area electron diffraction (SAED) patterns were acquired using a Themis 200 G3 aberration (probe)-corrected TEM (ThermoFischer) operating at 200 kV, equipped with a Nanomegas EDS system. Fast Fourier Transformed (FFT) images are generated from lattice fringes.

3. Results

The differences between the two samples (S1 and S2) were already introduced in Section 2.1, and shown in Fig. 1. Based on the chemical profiles measured by TOF-SIMS and TEM/EDS, it can be concluded that the composition of the FCC phase is not influenced by the cooling rate, while S1 differs from S2 in terms of the Cr-rich precipitates in the BCC matrix. Therefore, the most pronounced dissimilarities within the global mechanical response in these two materials are directly linked to the precipitates within the BCC phase. This effect can be further studied in case of the emerging size effects. As to the variance between the FCC/BCC small scale local mechanical properties, sample S1 was chosen to be the material where size and strain rate related effects are both discussed in this work, as the evaluation of such a rapidly cooled system is missing from the literature.

First, micropillars of ∼3 μm diameter were compressed and the analysed data showed a huge variety of stress-strain curves. The results can be categorized into two main groups, namely deformation curves of *(i)* pure BCC or FCC pillars, and *(ii)* mixed pillars, containing a phase boundary within the deformed volume. In Fig. 2a, the $\sigma_{\mathrm{eng}} - \varepsilon_{\mathrm{eng}}$ curves show a very distinctive response to external loading.

In the BCC phase (pillars B5 and B6), the yield stress reaches extremely high values after the elastic loading ($\varepsilon \sim 0.03$), that is followed by a rather smooth plastic regime. Around $\varepsilon \sim 0.08$, a load drop of ∼ 0.2 GPa indicates the activation of a slip plane, where the deformation continues, reducing the hardening rate afterwards. In pillar B5, a second slip is activated close to the maximum applied strain ($\varepsilon \sim 0.14$), while B6 is unloaded before this event.

Contrary to the BCC phase, the FCC pillars show much lower yield point ($\sim 200 - 300$ MPa), that is followed
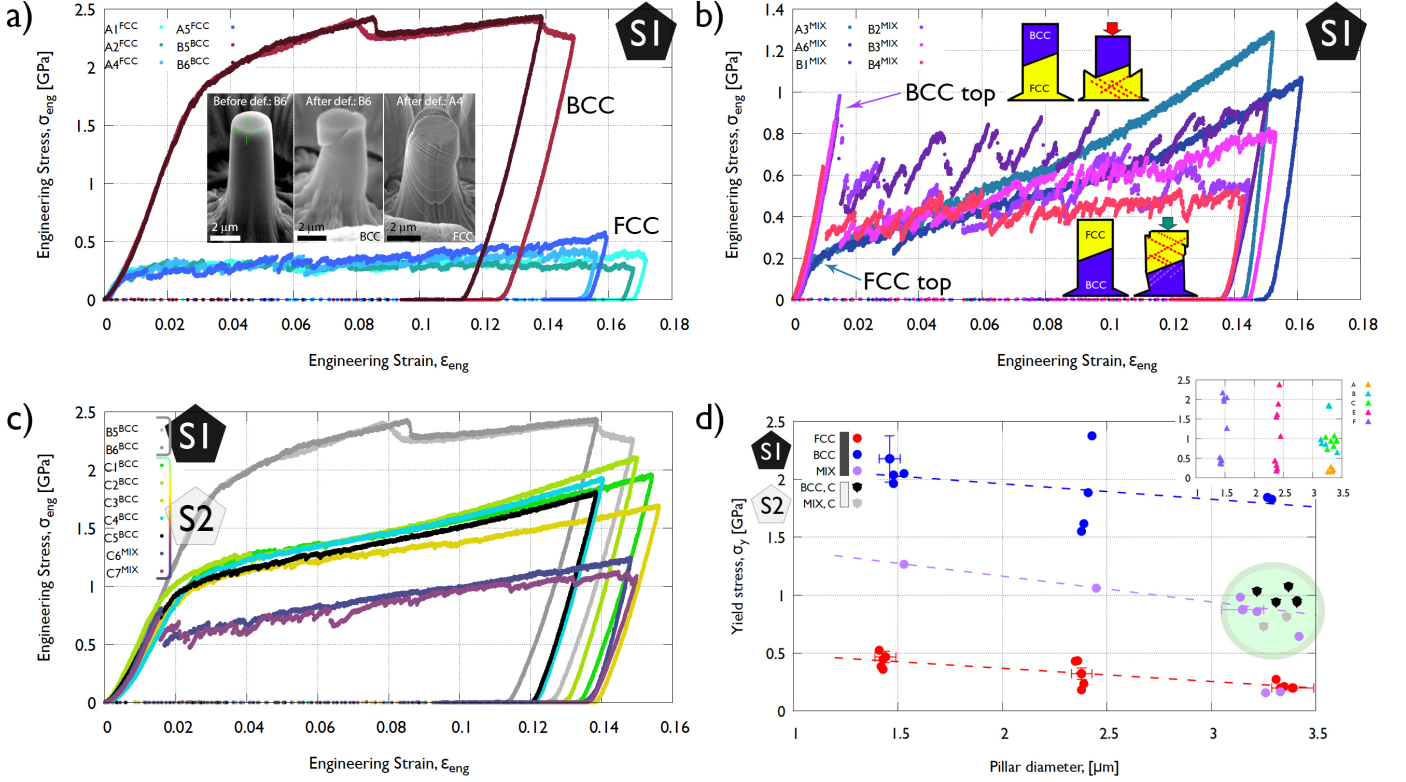
Figure 2: **Stress-strain plots at quasi-static SR** (d∼ 3 μm). **(a)** Pure FCC and BCC $\sigma_{eng} - \varepsilon_{eng}$ comparison, Sample 1. Inset images show the pillars before and after deformation. **(b)** Pillars with mixed phases, Sample 1. Insets showing the deformation mechanisms based on imaging mixed mode pillars after compression (see in Suppl. Fig. S12 and S13). **(c)** Deformation curves measured on BCC pillars on Sample 1 (S1: B5, B6) and Sample 2 (S2: C1-C7). **(d)** Yield stress dependency of the pillar diameter (*"size effect"*). The inset shows which point belongs to which set of pillars in Suppl. Tables S2 and S3.

by a jerky plastic part. The load drops indicate dislocation avalanches activated on the possible slip planes, that are confirmed by the *post mortem* imaging of the pillar surfaces meshed with numerous steps on their facets. Multiple slip planes are activated as a result of the achieved high maximum strains, that continuously produced dislocations to accommodate the shape change of the pillar. Secondary electron images of pillars before and after deformation are shown in the inset of Fig. 2a. The recorded pure deformation curves exhibit good repeatability, however, due to the small grain size (rapid cooling of S1), the microstructure holds a challenge to be evaluated by such large pillars, as phase boundaries can be included in the FIB-milled volumes. The presence of such boundaries are hidden until the pillars are deformed, or their cross-sections are analysed by another microstructure sensitive technique. As the latter was not possible in the current study before performing the compression tests, specimens were fabricated in larger numbers.

Pillars falling into the "mixed" category are plotted in Fig. 2b. Here, two characteristic behaviour can be observed. On the one hand, samples with BCC top / FCC bottom exhibit about 3-4 times higher yield point than pillars with reverse composition and the plastic regime is dominated by load drops characteristic to the FCC phase. These load drops are due to strain burst being activated in

the lower pillar volume. On the other hand, the strengths of the FCC top / BCC bottom pillars reach much higher values than previously seen, where stress drops are mainly apparent at the onset of plasticity and are relatively small. These results lead to the sketches shown in the insets of Fig. 2b, describing how mixed pillars deform under compression. Mixed pillars with BCC tops show no (or only very limited) slip activity in the upper region, while the bottom FCC part becomes dense in slip bands due to the dislocation activity (see Suppl. Fig. S12 red arrow and S13a. Pillars with FCC tops on the other hand start to slip immediately after elastic loading on the favoured slip planes. Generated dislocations begin to pile up against the phase boundaries, inducing a large strain field, that eventually can create new dislocations within the BCC lower region if the deformation is high enough (see Suppl. Figs. S12 green arrow and S13b.

The comparison of $\sigma_{eng} - \varepsilon_{eng}$ curves belonging to the S1 (BCC) and S2 (BCC and mixed: BCC top) samples are shown in Fig. 2c. In S2, the precipitates appearing in the BCC phase cause the high entropy mixture to reduce its yielding by ∼50%. By plotting the yield stress values as a function of the pillar diameters in Fig. 2d, one can observe that the S2 sample yields at similar values as S1 mixed pillars (green highlighted area) in case of the largest tested pillars. If one looks at how the pillar size affects

the yielding, a monotonous trend can be concluded, where the smaller pillars exhibit somewhat higher σ_y. As these samples are only minimally influenced by their size, pillars with the smallest diameters (but still above the regime where FIB-induced damage would be considerable) were chosen to investigate the strain rate sensitivity behaviour. This reduces the possibility to create and analyse mixed pillars. In Fig. 2d, the σ_y values for the mixed pillars were set as the maximum yield stress before the first load drop. In case of the other pillars, a linear fitting method (on both the elastic and plastic parts) were considered (see in Ref. [51] and in Fig. 3 on the BCC $\dot{\varepsilon} = 0.001/s$ curve) to be consistent with the more challenging high strain rate evaluation.

In Fig. 3, a few representative stress-strain curves of compressed micropillars are plotted, measured only on S1. It can be observed that with increasing strain rate, the noise on the experimental plots increase. This can be attributed to the application of various load sensors designed to operate under certain conditions. The oscillations appearing $\dot{\varepsilon} \sim 1000/s$ is related to the ringing effect.
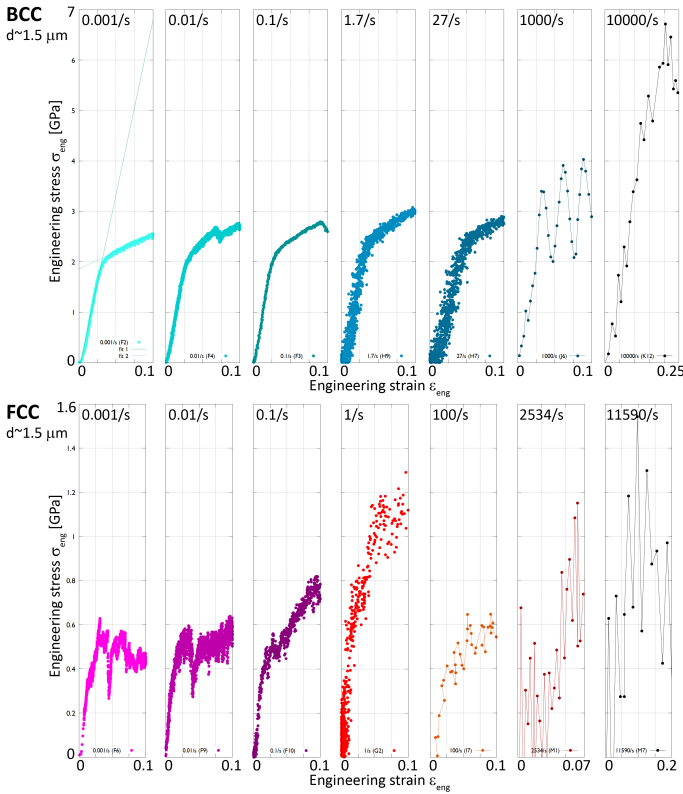
Figure 3: **Stress-strain curves** at various strain rates, Sample 1.

By extracting the yielding events from the $\sigma_{eng} - \varepsilon_{eng}$ curves, the SRS behaviour can be created in Figure 4, plotted in log-log scale for easier comprehension. The inset shows the log-log plot of the same dataset. Following the well-established strain rate sensitivity (m, [57]) calculation based on Eq. 1,

$$m = \frac{\partial(\ln \sigma)}{\partial(\ln \dot{\varepsilon})}, \qquad (1)$$

the SRS factors at each relevant interval (L: low strain rates, H: high strain rates) can be extracted for both BCC and FCC phases. For the construction of the SRS sensitivity behaviour, pillars with both 2.5 μm and 1.5 μm diameters were used.
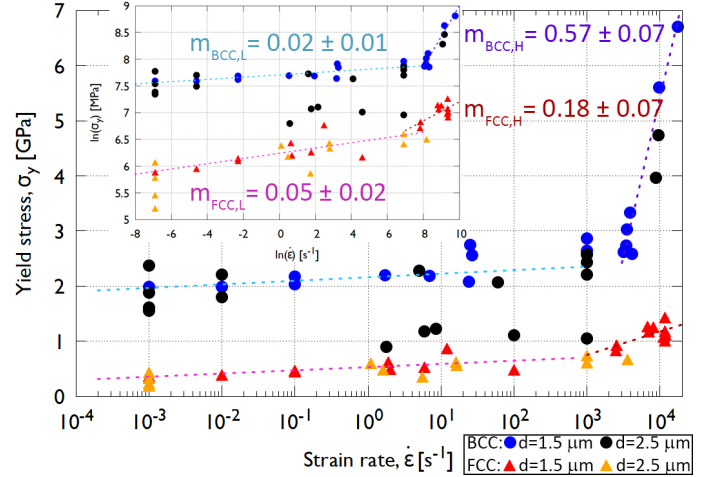
Figure 4: **Strain rate sensitivity:** The yield stress plotted as a function of the applied strain rate during compression, Sample 1, linear scaling. The inset shows the same dataset in log-log scale, that was used for the determination of the various m values.

After deformation, several pillars were lifted out for cross-sectional TEM analysis. In order to understand how dislocations interact with the precipitates forming in S2, dislocation characterization by bright field (BF) and dark field (DF) imaging were concluded in Figure 5 and in Suppl. Fig. S15. The TEM lamella was then mapped with HR-EBSD (transmission Kikuchi diffraction, HR-TKD) in the BCC phase, where Cr-rich cuboids are present. The consequent elastic strain (ε_{ij}) and rotation tensors (ω_{ij}) are plotted in Suppl. Fig. S20, while a Burgers vector analysis ([58, 59]) was performed in Suppl. Fig. S21. Pillars fabricated from S1 and deformed at various strain rates are also analyzed in Suppl. Fig. S16. Some pillars extracted from S1 were measured by HR-EBSD to confirm the constituent phases and to perform GND density and individual stress tensor mapping. These results are shown in Figure 6, Suppl. Fig. S7 and S8. The surface of Sample 2 was also mapped by HR-EBSD before deformation in order to determine preexisting stress localization and dislocation density (shown in Suppl. Fig. S17 and S18). A typical diffraction pattern in Suppl. Fig. S19 highlights the good surface quality prior to pillar fabrication in Sample 2.

4. Discussion

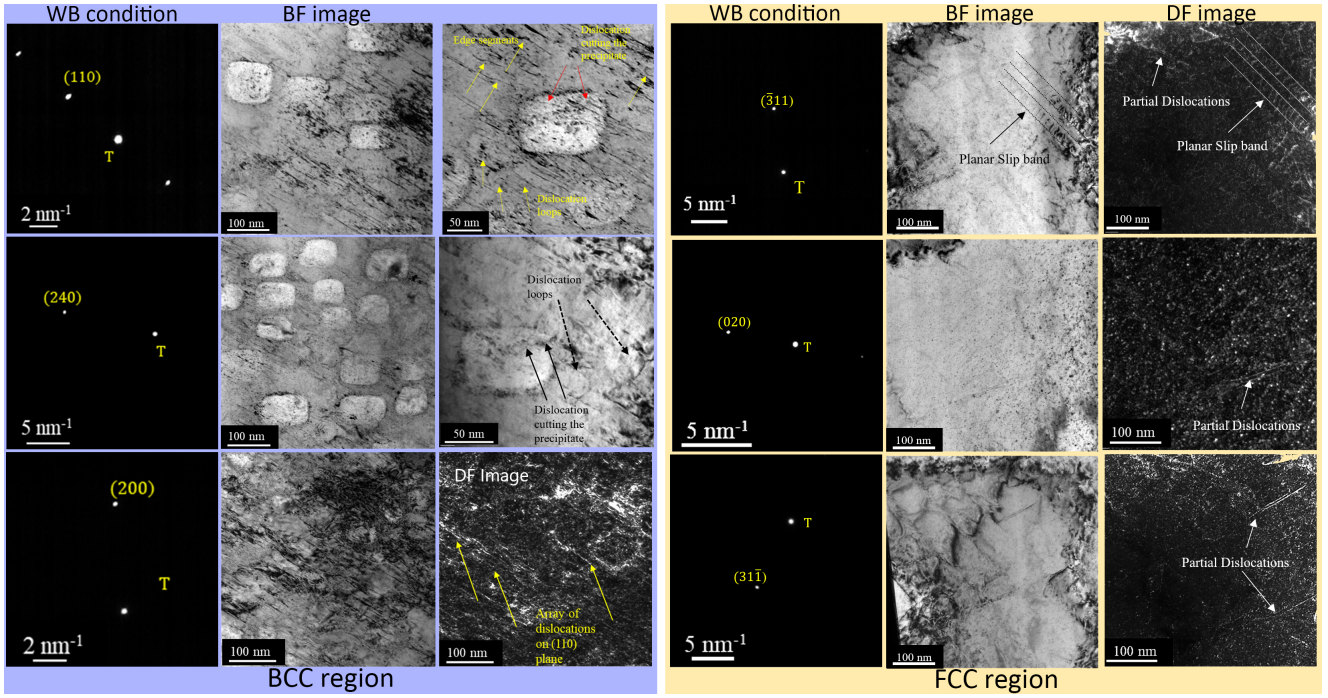In this work, the mechanical effects of the FCC and BCC phases (including precipitations) were studied at the

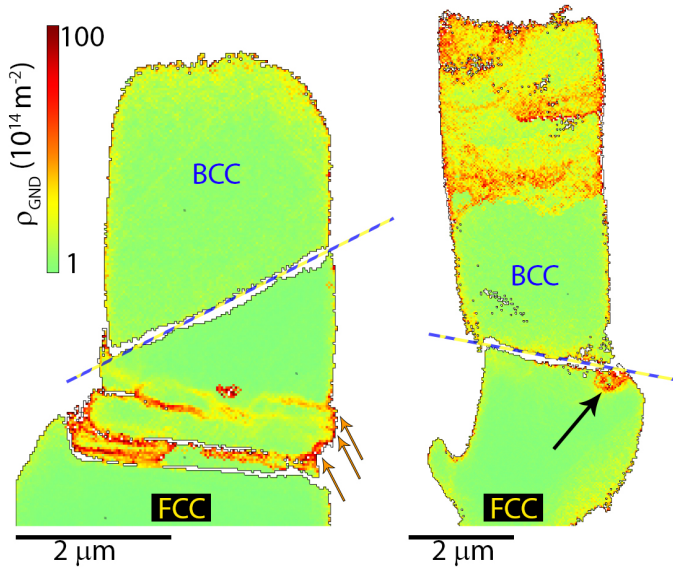Figure 5: **TEM, dislocations** after deformation of pillar C1 (Sample 2).

Figure 6: **HR-EBSD results,** Sample 1, cross-sectional GND density distributions measured on pillars (left) B3 and (right) B6. Conventional EBSD results are additionally shown in Suppl. Fig. S10 and S11.

micron scale, as the HEA's response to strain rates and sample sizes vary considerably. Two different heat treatments were used to create two distinct microstructures of the same compositionally complex alloy (S1 and S2).

Firstly, the mechanical response of two constituent phases were analyzed in S1 (FCC and BCC, Figure 2). Although the two phases were created from the same molten alloy (see in Fig. 1), there is a slight difference in their chemical composition (BCC is richer in Ni and Ga, but somewhat depleted of Cr), that is responsible for the variation in the final crystal structure. The BCC phase appears to be much harder than the FCC. If we apply longer heat treatment on the molten alloy (S2), the Cr in the BCC phase precipitates, that produces a BCC matrix with almost no residual Cr ($\sim 6\%$ based on TEM-EDS, hence the configurational entropy decreases in this phase), that further reduces the yielding point. From an engineering point of view, this decrease in σ_y is unfavourable in terms of performance (resistance to plastic deformation) and durability. However, understanding the mechanical characteristics of the constituents is key for phase engineering, that is especially consequential in case of mixed compositions with severely different properties. In our case, looking at the stress-strain responses, we can predict the composition of the deformed pillars without prior phase analysis.

4.1. Size effects

Size effects shown in Figure 2d seems to have no relation to the original crystal structure in S1 at the investigated length scale: both BCC and FCC have similar monotonous yield stress increase tendency towards smaller pillar sizes. Even though pillars were fabricated from differently oriented grains ([114], [104], [103], [102]), the results does not indicate a strong yield strength variation (see the inset of Figure 2d for pillar series identification). Usually the slight increase in σ_y with the decrease of the pillar diameter can be explained by the presence of significant dislocation density present in the deformed volume, that makes the defect source density high enough

8

to prevent a stochastic response. This could also be associated to a low scattering of the σ_y values no matter the sample size. To verify this, GND density measurements by HR-EBSD were carried out on the pristine material (shown in Suppl. Fig. S17). The mapping performed in S2 around phase boundaries showed similar and relatively high initial dislocation density in both FCC and BCC areas ($\overline{\rho_{GND}^{BCC}} = 1.05 \times 10^{14}$ m^{-2}, $\overline{\rho_{GND}^{FCC}} = 8.71 \times 10^{13}$ m^{-2}). Looking at the individual stress tensor components (Suppl. Fig. S18) it can be concluded that significant stress concentration (σ_{11}, σ_{22}) is located in the vicinity of the phase boundaries. Furthermore, the Cr-precipitation in the BCC section also appears to be acting as hotspots of such stresses. Local stresses (see i.e. σ_{12} and von Mises stress maps) can further modify dislocation behaviour at boundaries, that likely contribute to the detected $\sim 50\%$ decrease in yielding of S2 compared to the fast cooled S1 material, since less external load is required for dislocation activation due to already existing residual internal stresses.

The fitted size effect sensitivity values (from the dotted lines in Figure 2d) are: $\gamma^{BCC} = -0.13 \pm 0.11$, $\gamma^{FCC} = -0.11 \pm 0.02$, $\gamma^{MIXED} = -0.13 \pm 0.11$, that are considerably smaller than in other reported HEAs ($\sim 0.2 - 0.3$) [32, 60]. This is a clear indication that homogenization through extended heat treating will also increase the sensitivity of the material to the size of the sample. Earlier reported size effects in HEA micropillar compression tests show inconsistent results. In the range of 1-10 μm a power law relation with a log-log exponent of -0.32 was determined [30] in FCC single phase HEA, which is less significant than in pure FCC metals (~ -0.6) at high strain rates [24]. Here, in both BCC and FCC (and mixed) pillars, the γ parameter is the same within the error range, however, more scatter is detected in the BCC σ_y values.

4.2. Strain rate sensitivity

By studying the $\sigma_{eng} - \varepsilon_{eng}$ curves in Figure 3 and Suppl. Fig. S9, one can conclude increased strain hardening rates in the FCC phase with increasing $\dot{\varepsilon}$. Furthermore, the yielding point is typically reached at higher applied strains in both cases in the HSR regime. The oscillations caused by the ringing effect makes it more challenging to extract the exact σ_y values, but the applied linear fitting methods produces consistent and repeatable results. SR jump testing (SRJT) has its own limitations (Suppl. Fig. S10), as the applied sampling rate cannot be too different for the studied strain rates, since only one load cell is used during measurement, that is specific to a certain SR regime. SRJT performed on 2 μm diameter pillars (series E) confirmed that these pillars (FCC or BCC) does not show strong strain rate sensitivity (Suppl. Fig. S10c), that is in agreement with the conventional constant $\dot{\varepsilon}$ experimental results. This is expected from the literature [30], where it is shown that HEAs typically exhibit less significant strain rate effects than pure metals, while this behaviour can be attributed to the larger lattice distortion,

which affects the dislocation motion through the lattice friction (Peierls) stress.

After extracting the σ_y values and creating the SRS plot in Figure 4, the difference between the LSR and HSR regime behavior of the two phases are evident. In the BCC phase, the SRS factor exhibits a sharp increase above 10^3/s, transitioning from $m_{BCC,L} = 0.02 \pm 0.01$, $\dot{\varepsilon} \subset [10^{-3}, 10^3]$ to a compelling $m_{BCC,H} = 0.57 \pm 0.07, \dot{\varepsilon} \subset [3 \times 10^3, 2 \times 10^4]$, that is an approx. 28 fold increase. Similar behaviour has already been reported in bulk UHSR experiments [61, 62, 43] and by simulations [23], but not on the micro-scale before. The significance of performing such an experiment is to finally bridge experimentally (high) and computationally (low) achievable strain rates together on a similar length scale (i.e by discrete dislocations dynamics – DDD, or molecular dynamics – MD modelling). Looking at the FCC SRS factor, a less momentous ($\times 3.6$, about 8 times weaker than in BCC) transition occurs above 10^3/s SR, from $m_{FCC,L} = 0.05 \pm 0.02, \dot{\varepsilon} \subset [10^{-3}, 10^3]$ to $m_{FCC,H} = 0.18 \pm 0.07, \dot{\varepsilon} \subset [10^3, 2 \times 10^4]$. It is noteworthy that due to the generally lower yielding in this phase, the extraction of σ_y values is much more challenging. However, the multiple repetitions gave consistent reading on the final σ_y even when $\dot{\varepsilon} > 10^4$. The reason behind such transition in the SRS factor at HSR is generally considered to be the fact that in this deformation regime, dislocation movement is no longer only controlled by thermal activation (such as at LSR and low applied stresses) [63]. At HSR, dislocation motion is mostly drag controlled, that leads to the observed overdamped defect mobility as a result of interactions with lattice phonons and electrons [64]. Consequently, the viscous drag force will be proportional to the speed of dislocation in this regime [65], meaning that higher forces will be required to initiate dislocation motion upon loading, resulting in the increased yielding point.

It is worth mentioning that a few pillars that were originally classified as BCC with 2.5 μm diameter showed much lower yielding than expected ($\dot{\varepsilon} \subset [10^0, 10^3]$) as a result of being compositionally mixed (BCC top, FCC bottom), but they are still plotted in Figure 4. These pillars were excluded from the m determination.

There is no clear difference in the SRS between the larger (2.5 μm) and smaller (1.5 μm) pillars, however, as the larger pillars often contained a phase boundary, it was difficult to extract values for the pure phases (even when pillars were tested in such high numbers). The size reduction must certainly play a role in terms of the number of initially present dislocations. In the current work, it was impossible to study this effect due to the complex nature of the material and the challenging micromechanical testing. On the other hand, other groups have already looked into the theoretical background of dislocation density affecting the SRS of yielding, i.e. Fan et al. [23]. Researchers have applied DDD and MD simulations to predict the yielding of pure FCC (as in Cu single crystal) as a function of initial dislocation density. They have also identified a regime

around $10^3/s$, where σ_y increases substantially.

Based on these simulation results, we found our experimental outcome to be consistent with the theoretical prediction, namely that higher initial dislocation density (as expected in larger pillars) results in less significant SRS increase than in samples containing more mobile dislocations. This can be observed in Figure 4, where the σ_y values extracted from bigger pillars (black dots) are somewhat smaller than in case of the 1.5 μm pillars (blue dots) above $10^3/s$. The σ_y ratios are in accordance with the size effect measurements at lower strain rates, meaning that this phenomena is preserved (and monotonous) within the studied strain rate range.

One possible cause of the smaller SRS increase in FCC could be related to the difference in the initial dislocation density in this phase, therefore dislocation analysis by TEM was performed on compressed pillars of Sample 1 (shown in Suppl. Fig. S16) and in Sample 2 (in Figure 5 and Suppl. Fig. S15). Multiple pillars deformed to a lower maximum strain level were lifted out, that confirmed the presence of large amounts of dislocations within the investigated samples. Hence individual Burgers vector analysis was not possible by TEM in Sample 1.

The analysis of Sample 2 by TEM was more fruitful. Generally speaking, the appearance of precipitates could manifest in increased yielding in alloys (i.e. precipitation hardening). In our case, the Cr-rich cuboids in the BCC matrix induce the opposite: the yield stress values drop drastically in S2. As we look at the dislocation interactions with these precipitates in Figure 5, it can be observed that dislocations simply cut through the cuboids instead of being pinned down at the interfaces. Dislocations (both straight sections and loops) were observed using weak-beam (WB) diffraction conditions (bright field – BF, dark field – DF) by TEM in a micropillar (C1) compressed at LSR. HR-TEM analysis at the matrix-precipitate interface confirmed the coherent nature of the boundary (Suppl. Fig. S15), that facilitates dislocation crossing (hence the missing precipitation hardening effect). Contrary to an earlier TEM investigation performed on the same material [21], the extra diffraction spots corresponding to the Cr-rich cuboids were clearly identified on the fast Fourier transformed (FFT) imaging. It is interesting to mention the detection of lattice distortions in the HR-TEM matrix image, similarly to Ref. [32].

Some areas exhibited an array on dislocations on the (110) slip plane in the BCC region. The sample contained a phase boundary close to the bottom, that allowed TEM analysis on the FCC region too. In this phase, dislocation pile-ups were observed on planar slip bands, forming a more organized defect network. The ability of dislocations to freely move within this phase contributes to the decrease of σ_y and allows defects to escape the pillars though the surfaces. Partial dislocations were also detected in the FCC region, that is expected due to the generally lower stacking fault energy of FCC phase compared to BCC.

In order to have some information on the collective

Burgers vectors of the generated defects withing the BCC phase, HR-EBSD mapping was performed on the TEM lamella (also referred to as HR-TKD) of pillar C1. The resulting elastic strain (ε_{ij}) and rotation tensor (ω_{ij}) elements are plotted in Suppl. Figs. S20 and S21. It can be seen that the presence of precipitation (circled areas in Suppl. Fig. S21a) causes local strain variation both in the normal and shear strain maps. Components of the Nye dislocation density tensor (α_{i3}) can be calculated from the elements of the distortion tensor $\beta_{ij} = \partial_j u_i$, with $\boldsymbol{u}$ being the displacement field (accessible by HR-EBSD) as [66, 58]:

$$\alpha_{i3} = \partial_1 \beta_{i2} - \partial_2 \beta_{i1}, \quad i = 1, 2, 3. \qquad (2)$$

The resulting maps of α_{13} and α_{23} correspond to edge type dislocations, while the third component (α_{33}) shows screw type of GND features. Based on the HR-TKD analysis one can conclude that the majority of dislocations detected in the lamella were edge types, which is in agreement with the HR-TEM findings.

4.3. Microstructure effects

Two pillars (B3 and B6) from Sample 1 were further subjected to cross-sectional HR-EBSD analysis following the LSR compression experiments (Figure 6). From the GND density maps we can deduce that in case of a mixed composition within the pillar (BCC top, FCC bottom, B3), the hard BCC remains mostly dislocation free (however, a slight increase close to the flat punch / pillar interface can be detected). Upon reaching a critical external loading, the bottom FCC "collapses", producing larger amount of GNDs that easily move within this section, creating slip traces visible on the surface (marked with orange arrows). Experimental evidence was already provided in the literature for the tendency of FCC having more mobile dislocations (screw dislocations in BCC are harder to activate), resulting easier annihilation upon reaching the pillar surfaces [67, 68]. As a result, there is the difference in FCC/BCC hardening rates in the $\sigma_{eng} - \varepsilon_{eng}$ plots (see in Suppl. Fig. S9). To the contrary, BCC materials exhibit a dislocation self-multiplication mechanism [69, 70], that causes defects to multiply and form an entangled dislocation network before leaving the system. This difference is observable in the two pillars in Figure 6, where GNDs form clear line structure, whereas the BCC GND network is more homogeneously distributed.

On the other hand, if the pillar was pure BCC along the whole thickness (B6, where the phase boundary is located just below the base of the pillar), the BCC phase shows increased GND activity in its upper section. However, as this part is pushed into the softer FCC base, dislocation initiation in the bottom region can be observed too (marked by a black arrow). This image was captured just at the onset of GND initiation within the FCC phase.

10

5. Conclusions

In summary, the current study presents straightforward results on the size and strain rate sensitivity of a eqiumolar (NiCoFeCrGa) high entropy alloy composed of a mixture of BCC/FCC phases. The constituent phases were studied in the mechanical context individually (by deforming pure BCC/FCC pillars), and in case of mixed compositions (pillars with BCC/FCC top-bottom configurations). The current work provides the first clear micromechanical experimental evidence of a transition between thermally activated and drag-controlled deformation mechanisms in FCC and BCC structures. At low strain rates, the thermally activated dislocation motion manifests in weak and monotonous strain rate sensitivity in both BCC and FCC phases. Exceeding the $10^3/s$ strain rate, the drag effect becomes dominant, leading to a sharp increase in the yield stress values. This effect is about 8 times stronger in the BCC phase, that can be attributed to the difference in dislocation characteristics. The measurements are reproducible, and similar tends between experiments and earlier simulation results can be established.

CRediT author statement

S. Kalácska: conceptualization, methodology, validation, formal analysis, investigation, writing – original draft, writing – review & editing, visualization, project administration, funding acquisition, supervision, **A. Sharma:** validation, investigation, writing - review & editing, **R. Ramachandramoorthy:** investigation, writing – review & editing, **Á. Vida:** writing – review & editing, **F. Tropper:** investigation, **R. Pero:** resources, **D. Frey:** resources, **J. Michler:** funding acquisition, writing – review & editing, **X. Maeder:** funding acquisition, writing – review & editing, **P. D. Ispánovity:** writing – original draft, writing – review & editing, **G. Kermouche:** formal analysis, funding acquisition, writing – original draft, writing – review & editing.

Competing interests

The authors declare that they have no known competing financial interests or personal relationships that could have appeared to influence the work reported in this paper.

Supporting Information

Supporting Information and all data are available at the Zenodo repository or from the corresponding author upon reasonable request.

References

[1] J. W. Yeh, S. K. Chen, S. J. Lin, J. Y. Gan, T. S. Chin, T. T. Shun, C. H. Tsau, S. Y. Chang, Nanostructured High-Entropy Alloys with Multiple Principal Elements: Novel Alloy Design Concepts and Outcomes, Adv. Eng. Mat. 6 (5) (2004) 299–303. doi:10.1002/adem.200300567.

[2] B. Cantor, I. T. H. Chang, P. Knight, A. J. B. Vincent, Microstructural development in equiatomic multicomponent alloys, Adv. Eng. Mat. 375-377 (2004) 213–218. doi:10.1016/j.msea.2003.10.257.

[3] D. Miracle, High entropy alloys as a bold step forward in alloy development, Nature communications 10 (1) (2019) 1805.

[4] E. P. George, W. Curtin, C. C. Tasan, High entropy alloys: A focused review of mechanical properties and deformation mechanisms, Acta Materialia 188 (2020) 435–474.

[5] M.-H. Tsai, J.-W. Yeh, High-entropy alloys: a critical review, Materials Research Letters 2 (3) (2014) 107–123.

[6] D. B. Miracle, High-Entropy Alloys: A Current Evaluation of Founding Ideas and Core Effects and Exploring Nonlinear Alloys, Journal of Microscopy 69 (2017) 2130–2136. doi:10.1007/s11837-017-2527-z.

[7] O. El-Atwani, N. Li, M. Li, A. Devaraj, J. Baldwin, M. Schneider, D. Sobieraj, J. S. Wróbel, D. Nguyen-Manh, S. Maloy, E. Martinez, Outstanding radiation resistance of tungsten-based high-entropy alloys, Science Advances 5 (3) (2019). doi:10.1126/sciadv.aav2002.

[8] E. Ma, X. Wu, Tailoring heterogeneities in high-entropy alloys to promote strength–ductility synergy, Nature communications 10 (1) (2019) 5623.

[9] R. Feng, C. Zhang, M. C. Gao, Z. Pei, F. Zhang, Y. Chen, D. Ma, K. An, J. D. Poplawsky, L. Ouyang, et al., High-throughput design of high-performance lightweight high-entropy alloys, Nature Communications 12 (1) (2021) 4329.

[10] D. B. Miracle, O. N. Senkov, A critical review of high entropy alloys and related concepts, Acta Materialia 122 (2017) 448–511. doi:10.1016/j.actamat.2016.08.081.

[11] H.-W. Luan, Y. Shao, J.-F. Li, W.-L. Mao, Z.-D. Han, C. Shao, K.-F. Yao, Phase stabilities of high entropy alloys, Scripta Materialia 179 (2020) 40–44.

[12] X. Chang, M. Zeng, K. Liu, L. Fu, Phase engineering of high-entropy alloys, Advanced Materials 32 (14) (2020) 1907226.

[13] S. Gou, M. Gao, Y. Shi, S. Li, Y. Fang, X. Chen, H. Chen, W. Yin, J. Liu, Z. Lei, H. Wang, Additive manufacturing of ductile refractory high-entropy alloys via phase engineering, Acta Materialia 248 (2023) 118781. doi:10.1016/j.actamat.2023.118781.

[14] O. Senkov, G. Wilks, D. Miracle, C. Chuang, P. Liaw, Refractory high-entropy alloys, Intermetallics 18 (9) (2010) 1758–1765.

[15] S. Chen, W. Li, X. Xie, J. Brechtl, B. Chen, P. Li, G. Zhao, F. Yang, J. Qiao, P. K. Liaw, Nanoscale serration and creep characteristics of al0. 5cocrcufeni high-entropy alloys, Journal of Alloys and Compounds 752 (2018) 464–475.

[16] Y. Y. Chen, J. H.Li, S. Y. Tung, M. H. Tsai, On the phase constituents of three CoCrFeNiX (X = B, Al, Ga) high-entropy alloys after prolonged annealing, Journal of Alloys and Compounds 900 (2022) 163388. doi:10.1016/j.jallcom.2021.163388.

[17] S. Huang, A. Vida, W. Li, D. Molnár, S. K. Kwon, E. Holm-ström, B. Varga, L. K. Varga, L. Vitos, Thermal expansion in FeCrCoNiGa high-entropy alloy from theory and experiment, Appl. Phys. Lett. 110 (2017) 241902. `doi:10.1063/1.4985724`.

[18] A. Vida, L. K. Varga, N. Q. Chinh, D. Molnar, S. Huang, L. Vi-tos, Effects of the sp element additions on the microstructure and mechanical properties of NiCoFeCr based high entropy al-loys, Mat. Sci. Eng. A 669 (2016) 14–19. `doi:10.1016/j.msea.2016.05.082`.

[19] A. Vida, Z. Maksa, D. Molnár, S. Huang, J. Kovac, L. K. Varga, L. Vitos, N. Q. Chinh, Evolution of the phase structure after different heat treatments in NiCoFeCrGa high entropy alloy, Journal of Alloys and Compounds 743 (2018) 234–239. `doi:10.1016/j.jallcom.2018.01.407`.

[20] D. Molnár, A. Vida, S. Huang, N. Q. Chinh, The effect of cool-ing rate on the microstructure and mechanical properties of NiCoFeCrGa high-entropy alloy, Journal of Materials Science 54 (2019) 5074–5082. `doi:10.1007/s10853-018-03196-8`.

[21] Ádám Vida, J. Lábár, Z. Dankházi, Z. Maksa, D. Molnár, L. K. Varga, S. Kalácska, M. Windisch, G. Huhn, N. Q. Chinh, A Sequence of Phase Transformations and Phases in NiCoFeCrGa High Entropy Alloy, Materials 14 (5) (2021) 1046. `doi:10.3390/ma14051076`.

[22] G. Guillonneau, M. Mieszala, J. Wehrs, J. Schwiedrzik, S. Grop, D. Frey, L. Philippe, J. Breguet, J. Michler, J. Wheeler, Nanomechanical testing at high strain rates: New instrumen-tation for nanoindentation and microcompression, Materials & Design 148 (2018) 39–48. `doi:10.1016/j.matdes.2018.03.050`.

[23] H. Fan, Q. Wang, J. A. El-Awady, D. Raabe, M. Zaiser, Strain rate dependency of dislocation plasticity, Nature Communica-tion 12 (2021) 1845. `doi:10.1038/s41467-021-21939-1`.

[24] Y. Zou, Nanomechanical studies of high-entropy alloys, J. Mater. Res. 33 (19) (2018) 3035–3054. `doi:10.1557/jmr.2018.155`.

[25] A. Heczel, M. Kawasaki, D. Ugi, J. Jang, T. G. Langdon, J. Gubicza, The influence of chemical heterogeneities on the local mechanical behavior of a high-entropy alloy: A micropil-lar compression study, Mat. Sci. Eng. A 721 (2018) 165–167. `doi:10.1016/j.msea.2018.02.087`.

[26] M. Alfreider, M. Meindlhumer, V. Maier-Kiener, A. Hohen-warter, D. Kiener, Extracting information from noisy data: strain mapping during dynamic in situ SEM experiments, Jour-nal of Materials Research 36 (2021) 2291–2304. `doi:10.1557/s43578-020-00041-0`.

[27] J. Yan, S. Yin, M. Asta, R. Ritchie, J. Ding, Q. Yu, Anomalous size effect on yield strength enabled by compositional hetero-geneity in high-entropy alloy nanoparticles, Nature Comm. 13 (2022) 2789. `doi:10.1038/s41467-022-30524-z`.

[28] S. Peng, K. Jin, X. Yi, Z. Dong, X. Guo, Y. Liu, Y. Cheng, N. Jia, H. Duan, J. Xue, Mechanical behavior of the HfNbZrTi high entropy alloy after ion irradiation based on micro-pillar compression tests, Journal of Alloys and Compounds 892 (2022) 162043. `doi:10.1016/j.jallcom.2021.162043`.

[29] Y. Chen, X. An, S. Zhanga, F. Fang, W. Huo, P. Munroe, Z. Xie, Mechanical size effect of eutectic high entropy alloy: Effect of lamellar orientation, Journal of Materials Science & Technology 82 (2021) 10–20. `doi:10.1016/j.jmst.2020.11.067`.

[30] R. Raghavan, C. Kirchlechner, B. Jaya, M. Feuerbacher, G.Dehm, Mechanical size effects in a single crystalline equiatomic fecrcomnni high entropy alloy, Scripta Materialia 129 (2022) 52–55. `doi:10.1016/j.scriptamat.2016.10.026`.

[31] I. Basu, V. Ocelík, J. D. Hosson, Size effects on plasticity in high-entropy alloys, Journal of Materials Research 33 (2018) 3055–3076. `doi:10.1557/jmr.2018.282`.

[32] Y. Zou, S. Maiti, W. Steurer, R. Spolenak, Size-dependent plasticity in an $Nb_{25}Mo_{25}Ta_{25}W_{25}$ refractory high-entropy al-loy, Acta Materialia 65 (2014) 85–97. `doi:10.1016/j.actamat.2013.11.049`.

[33] R. Soler, A. Evirgen, M. Yao, C. Kirchlechner, F. Stein, M. Feuerbacher, D. Raabe, G. Dehm, Microstructural and me-chanical characterization of an equiatomic YGdTbDyHo high entropy alloy with hexagonal close-packed structure, Acta Ma-terialia 156 (2018) 86–96. `doi:10.1016/j.actamat.2018.06.010`.

[34] Y. Zhao, X. Wang, T. Cao, J. Han, M. Kawasaki, J. Jang, H. Han, U. Ramamurty, L. Wang, Y. Xue, Effect of grain size on the strain rate sensitivity of CoCrFeNi high-entropy alloy, Mat. Sci. Eng. A 782 (2020) 139281. `doi:10.1016/j.msea.2020.139281`.

[35] Y. Zou, H. Ma, R. Spolenak, Ultrastrong ductile and stable high-entropy alloys at small scales, Nature Communications 6 (1) (2015) 1–8. `doi:10.1038/ncomms8748`.

[36] C. Varvenne, A. Luque, W. A. Curtin, Theory of strengthening in fcc high entropy alloys, Acta Materialia 118 (2016) 164–176. `doi:10.1016/j.actamat.2016.07.040`.

[37] P. A. Geslin, A. Rida, D. Rodney, Microelasticity model of ran-dom alloys. Part II: displacement and stress correlations, Jour-nal of the Mechanics and Physics of Solids 153 (2021) 104480. `doi:10.1016/j.jmps.2021.104480`.

[38] Q. Ding, Y. Zhang, X. Chen, X. Fu, D. Chen, S. Chen, L. Gu, F. Wei, H. Bei, Y. Gao, M. Wen, J. Li, Z. Zhang, T. Zhu, R. Ritchie, Q. Yu, Tuning element distribution, structure and properties by composition in high-entropy alloys, Nature 574 (2019) 223–227. `doi:10.1038/s41586-019-1617-1`.

[39] R. Zhang, S. Zhao, J. Ding, Y. Chong, T. Jia, C. Ophus, M. Asta, R. Ritchie, A. Minor, Short-range order and its im-pact on the CrCoNi medium-entropy alloy, Nature 581 (2020) 283–287. `doi:10.1038/s41586-020-2275-z`.

[40] G. Muthupandi, K. R. Lim, Y. S. Na, J. Park, D. Lee, H. Kim, S. Park, Y. S. Choi, Pile-up and sink-in nanoindentation be-haviors in AlCoCrFeNi multi-phase high entropy alloy, Mat. Sci. Eng. A 696 (2017) 146–154. `doi:10.1016/j.msea.2017.04.045`.

[41] S. Sinha, R. A. Mirshams, T. Wang, S. S. Nene, M. Frank, K. Liu, R. S. Mishra, Nanoindentation behavior of high entropy alloys with transformation-induced plasticity, Sci. Rep. 9 (2019) 6639. `doi:10.1038/s41598-019-43174-x`.

[42] Z. M. Jiao, Z. H. Wang, R. F. Wu, J. W. Qiao, Strain rate sensitivity of nanoindentation creep in an AlCoCrFeNi high-entropy alloy, Appl. Phys. A 122 (2016) 794. `doi:10.1007/s00339-016-0339-6`.

[43] N. Kumar, Q. Ying, X. Nie, R. Mishra, Z. Tang, P. Liaw, R. Brennan, K. Doherty, K. Cho, High strain-rate compressive deformation behavior of the Al0.1CrFeCoNi high entropy alloy, Materials & Design 86 (2015) 598–602. `doi:10.1016/j.matdes.2015.07.161`.

[44] J. He, Q. Wang, H. Zhang, L. Dai, T. Mukai, Y. Wu, X. Liu, H. Wang, T. G. Nieh, Z. Lu, Dynamic deformation behavior of a face-centered cubic FeCoNiCrMn high-entropy alloy, Science Bulletin 63 (6) (2018) 362–368. `doi:10.1016/j.scib.2018.01.022`.

[45] S. Gangireddy, B. Gwalani, R. S. Mishra, Grain size dependence of strain rate sensitivity in a single phase FCC high entropy alloy Al0.3CoCrFeNi, Mat. Sci. Eng. A 736 (2018) 344–348. `doi:10.1016/j.msea.2018.09.009`.

[46] S. Gangireddy, L. Kaimiao, B. Gwalani, R. S. Mishra, Mi-crostructural dependence of strain rate sensitivity in thermo-mechanically processed Al0.1CoCrFeNi high entropy alloy, Mat. Sci. Eng. An 727 (2018) 148–159. `doi:10.1016/j.msea.2018.04.108`.

[47] M. Sadeghilaridjani, S. Muskeri, V. Hasannaeimi, M. Pole, S. Mukherjee, Strain rate sensitivity of a novel refractory high entropy alloy: Intrinsic versus extrinsic effects, Mat. Sci. Eng. A 766 (2019) 138326. `doi:10.1016/j.msea.2019.138326`.

[48] R. Ramachandramoorthy, F. Yang, D. Casari, M. Stolpe, M. Jain, J. Schwiedrzik, J. Michler, J. Kruzic, J. Best, High strain rate in situ micropillar compression of a Zr-based metallic glass, Journal of Materials Research 36 (11) (2021) 2325–2336. `doi:10.1557/s43578-021-00187-5`.

[49] R. Ramachandramoorthy, J. Schwiedrzik, L. Petho, C. Guerra-Nunez, D. Frey, J.-M. Breguet, J. Michler, Dynamic plasticity and failure of microscale glass: Rate-dependent ductile-brittle-ductile transition, Nanoletters 19 (4) (2019) 2350–2359. `doi:`

10.1021/acs.nanolett.8b05024.

[50] R. Ramachandramoorthy, S. Kalacska, G. Poras, J. Schwiedrzik, T. Edwards, X. Maeder, T. Merle, G. Ercolano, W. Koelmans, J. Michler, Anomalous high strain rate compressive behavior of additively manufactured copper micropillars, Applied Materials Today 27 (2022) 101415. doi:10.1016/j.apmt.2022.101415.

[51] S. Kalácska, L. Pethö, G. Kermouche, J. Michler, P. D. Ispánovity, Anomalous strain rate sensitivity of a Cu/Al_2O_3 multi-layered thin film, ArXiv Preprint (2024) 2407.21392doi:10.48550/arXiv.2407.21392.

[52] S. Huang, A. Vida, W. Li, D. Molnár, S. K. Kwon, E. Holmström, B. Varga, L. K. Varga, L. Vitos, Thermal expansion in FeCrCoNiGa high-entropy alloy from theory and experiment, Appl. Phys. Lett. 110 (2017) 241902. doi:10.1063/1.4985724.

[53] D. Dunn, R. Hull, Reconstruction of three-dimensional chemistry and geometry using focused ion beam microscopy, Appl. Phys. Lett. 75 (1999) 3414. doi:10.1063/1.125311.

[54] L. Giannuzzi, F. Stevie, Introduction to focused ion beams: instrumentation, theory, techniques and practice, Springer, 2004.

[55] L. Pillatsch, S. Kalácska, X. Maeder, J. Michler, In situ atomic force microscopy depth-corrected three-dimensional focused ion beam based time-of-flight secondary ion mass spectroscopy: Spatial resolution, surface roughness, oxidation, Microsc. and Microan. 27 (1) (2020) 65–73. doi:10.1017/S1431927620024678.

[56] A. Priebe, I. Utke, L. Pethö, J. Michler, Application of a gas-injection system during the FIB-TOF-SIMS analysis—influence of water vapor and fluorine gas on secondary ion signals and sputtering rates, Anal. Chem. 91 (18) (2019) 11712–11722. doi:10.1021/acs.analchem.9b02287.

[57] D. Caillard, J. Martin, Thermally Activated Mechanisms in Crystal Plasticity, Vol. 8, Pergamon Materials Series, 2003.

[58] S. Kalácska, Z. Dankházi, G. Zilahi, X. Maeder, J. Michler, P. D. Ispánovity, I. Groma, Investigation of geometrically necessary dislocation structures in compressed cu micropillars by 3-dimensional hr-ebsd, Mat. Sci. Eng. A 770 (2020) 138499. doi:10.1016/j.msea.2019.138499.

[59] S. Kalácska, J. Ast, P. D. Ispánovity, J. Michler, X. Maeder, 3D HR-EBSD characterization of the plastic zone around crack tips in tungsten single crystals at the micron scale, Acta Materialia 200 (2020) 211–222. doi:10.1016/j.actamat.2020.09.009.

[60] Y. Xiao, R. Kozak, M. J. R. Haché, W. Steurer, R. Spolenak, J. M. Wheeler, Y. Zou, Micro-compression studies of face-centered cubic and body-centered cubic high-entropy alloys: Size-dependent strength, strain rate sensitivity, and activation volumes, Mat. Sci. Eng. A. 790 (2020) 139429. doi:10.1016/j.msea.2020.139429.

[61] P. Follansbee, U. Kocks, A constitutive description of the deformation of copper based on the use of the mechanical threshold stress as an internal state variable, Acta Metallurgica 36 (1) (1988) 81–93. doi:10.1016/0001-6160(88)90030-2.

[62] D. Rittel, G. Ravichandran, A. Venkert, The mechanical response of pure iron at high strain rates under dominant shear, Mat. Sci. Eng. A 432 (1-2) (2006) 191–201. doi:10.1016/j.msea.2006.05.154.

[63] F. C. Salvado, F. Teixeira-Dias, S. M. Walley, L. J. Lea, J. B. Cardoso, A review on the strain rate dependency of the dynamic viscoplastic response of FCC metals, Progress in Materials Science 88 (2017) 186–231. doi:10.1016/j.pmatsci.2017.04.004.

[64] B. Gurrutxaga-Lermau, The role of the mobility law of dislocations in the plastic response of shock loaded pure metals, Modelling Simul. Mater. Sci. Eng 24 (2016) 065006. doi:10.1088/0965-0393/24/6/065006.

[65] B. Gurrutxaga-Lermau, D. S. Balint, D. Dine, D. Eakins, E. P. Sutton, Dynamic discrete dislocation plasticity, Advances in Appleid Mechanics (2014) 93–224doi:10.1016/B978-0-12-800130-1.00002-3.

[66] A. Wilkinson, D. Dingley, G. Meaden, Strain mapping using electron backscatter diffraction, in: A.J. Schwatz, M. Kumar, B.L. Adams, D.P. Field (Eds.) Electron Backscatter Diffraction in Materials Science), Springer Science+Business Media, 2009. doi:10.1007/978-0-387-88136-217.

[67] J. Greer, W. D. Nix, Nanoscale gold pillars strengthened through dislocation starvation, Phys. Rev. B 73 (2006) 245410. doi:10.1103/PhysRevB.73.245410.

[68] D. Kiener, A. M. Minor, Source truncation and exhaustion: Insights from quantitative in situ tem tensile testing, Nano Letter 11 (2011) 3816–3820. doi:10.1021/nl201890s.

[69] J. Greer, C. R. Weinberger, W. Cai, Comparing the strength of f.c.c. and b.c.c. sub-micrometer pillars: Compression experiments and dislocation dynamics simulations, Materials Science and Engineering: A 493 (2008) 21–25. doi:10.1016/j.msea.2007.08.093.

[70] C. R. Weinberger, W. Cai, Surface-controlled dislocation multiplication in metal micropillars, PNAS 105 (2008) 14304–14307. doi:10.1073/pnas.0806118105.

[71] Goodfellow materials catalogue, goodfellow.com.

Micromechanics reveal strain rate dependent transition between dislocation mechanisms in a dual phase high entropy alloy

Szilvia Kalácska[a,b,*], Amit Sharma[b], Rajaprakash Ramachandramoorthy[b,c], Ádám Vida[d], Florian Tropper[e], Renato Pero[e], Damian Frey[e], Xavier Maeder[b], Johann Michler[b], Péter Dusán Ispánovity[f], Guillaume Kermouche[a]

[a] *Mines Saint-Etienne, Univ Lyon, CNRS, UMR 5307 LGF, Centre SMS, 158 cours Fauriel 42023 Saint-Étienne, France*
[b] *Empa, Swiss Federal Laboratories for Materials Science and Technology, Laboratory of Mechanics of Materials and Nanostructures, CH-3602 Thun, Feuerwerkerstrasse 39. Switzerland*
[c] *Max-Planck-Institute für Eisenforschung, Max Planck Strasse 1, 40472 Düsseldorf, Germany*
[d] *Dept. of Industrial Materials Technology, Bay Zoltán Nonprofit Ltd. for Applied Research, Kondorfa u.1., H-1116 Budapest, Hungary*
[e] *Alemnis AG, Business Park Gwatt, Schorenstrasse 39, 3645 Gwatt (Thun), Switzerland*
[f] *ELTE Eötvös Loránd University, Department of Materials Physics, Pázmány Péter sétány 1/a, 1117 Budapest, Hungary*

S1. Microstructure characterization

Sample name	Phase ID	GAD (μm)	Mean (μm)	Min. (μm)	Max. (μm)	SD (μm)
S1	FCC	18.64	45.27	5.35	97.92	14.41
S1	BCC	25.52	107.66	5.35	174.72	30.9
S2	FCC	87.92	476.19	10	2127	184.95
S2	BCC	208	1658.86	10	5610	550.69

Suppl. Table S1: Grain statistics from large area EBSD maps, determined using AZtecCrystal v2.2. GAD: grain average diameter based on equivalent circle diameter, SD: standard deviation.
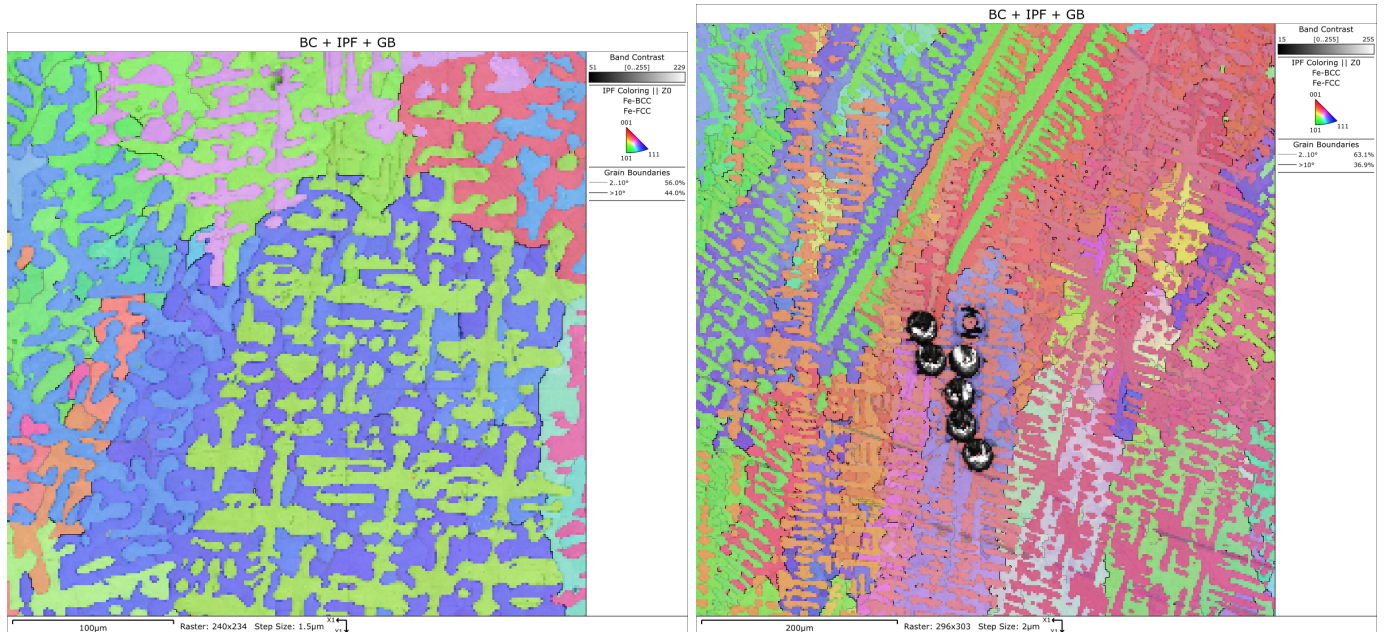
Suppl. Figure S1: Large area EBSD maps for grain statistics. (left) Sample 1, (right) Sample 2 mapped with the first pillars. BC: band contrast, IPF: inverse pole figure in Z direction, GB: grain boundaries.
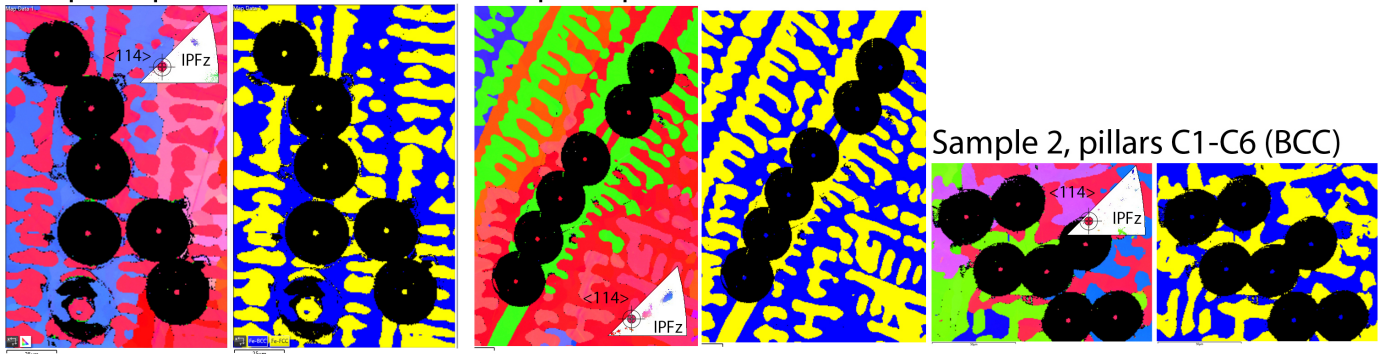
S2. Sample preparation
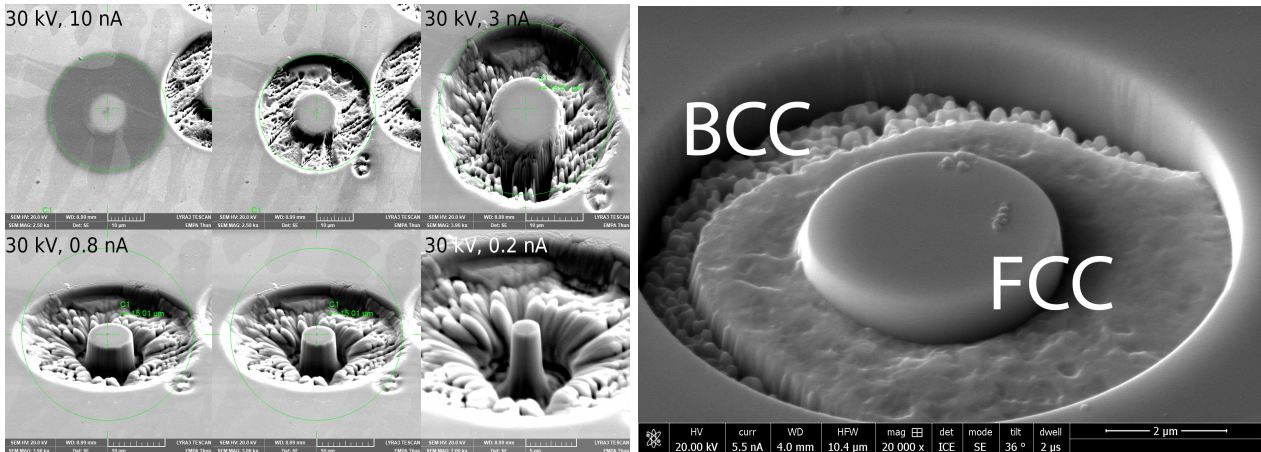
Suppl. Figure S2: (left) **Pillar fabrication, Sample 1.** (right) **Difference in sputtering speed between BCC and FCC phases.** SE image was take during pillar preparation (F7). The inner part is FCC, and the outer part of the crater overlaps with a BCC boundary. Image was taken at a 36° tilt with a 16° pre-tilted holder).
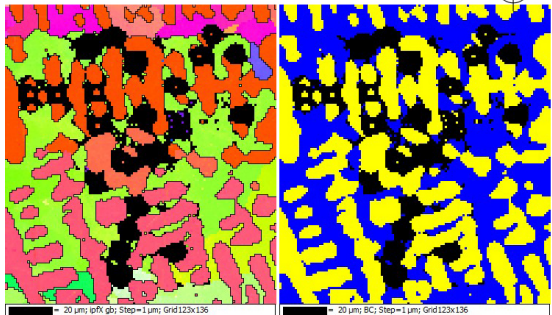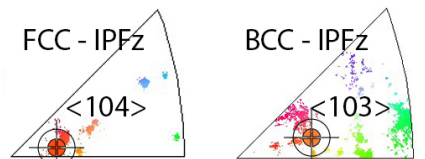

Suppl. Figure S3: **Pillars, series A, B, C**, Sample 1. IPF and phase maps of the three kinds of pillars prepared. Standard IPF triangles show only the pixels belonging to the pillar's phase. Phase map colors: FCC – yellow, BCC – blue.
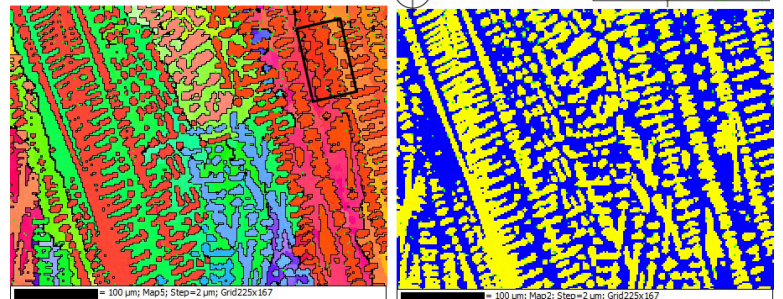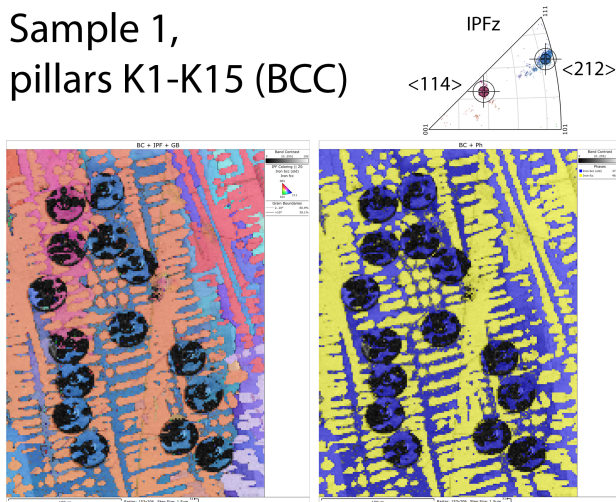

Suppl. Figure S4: **Pillars, series E, F, G, H**, Sample 1. IPF and phase maps of the two kinds of pillars prepared. Black square marks the final position of the pillar series G and H. Phase map colors: FCC – yellow, BCC – blue.

15
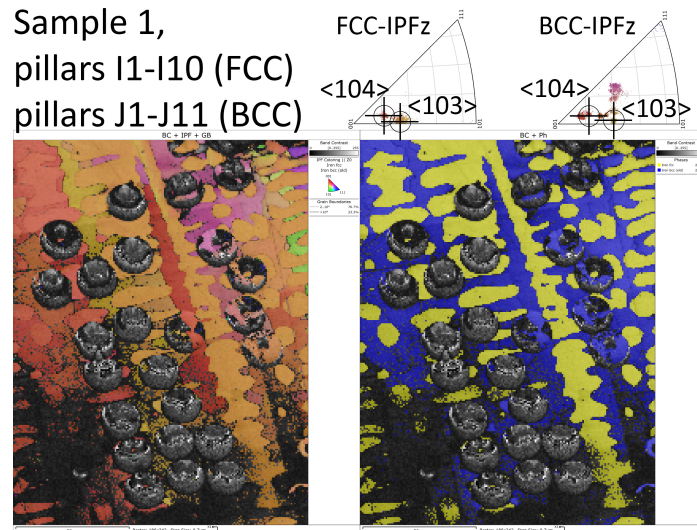
Suppl. Figure S5: **Pillars, series I and J**, Sample 1. IPF and phase maps of the BCC pillars prepared. Phase map colors: FCC – yellow, BCC – blue.
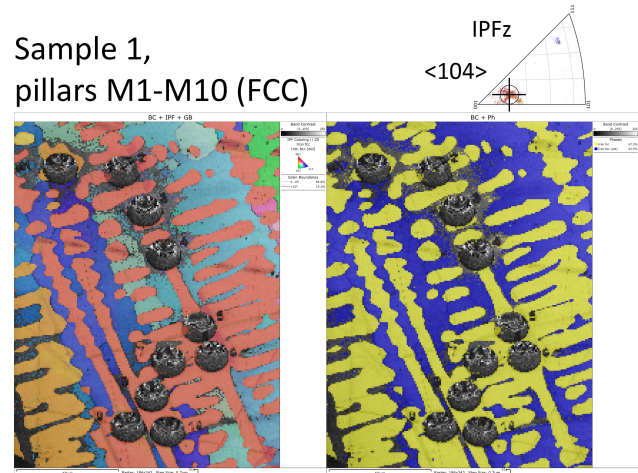
Suppl. Figure S6: **Pillars, series K and M**, Sample 1. IPF and phase maps of the BCC pillars prepared. Phase map colors: FCC – yellow, BCC – blue.
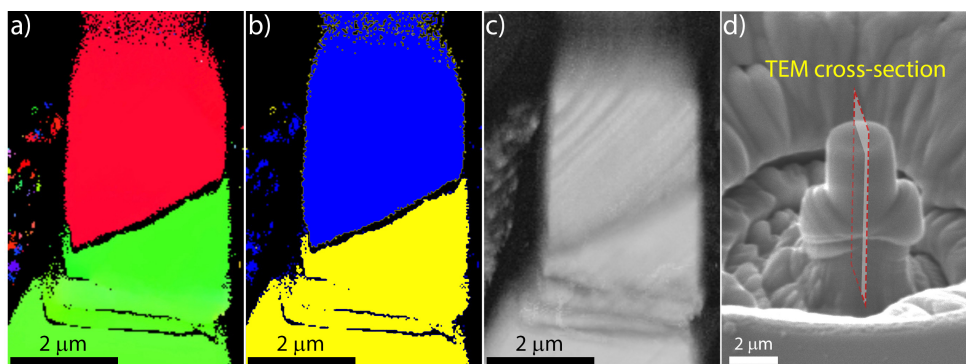
Suppl. Figure S7: **EBSD results**, Sample 1, pillar B3. (a) IPF-Y orientation map (coordinate-system origin is at the bottom left corner: X pointing towards the right, Y pointing upwards). (b) Phase map with colors: FCC – yellow, BCC – blue. (c) Band contrast image. FIB milling curtaining effect (with ~ 42° angle w.r.t. the horizontal direction) can be observed. (d) TEM cross-section plane sketched over the deformed pillar.
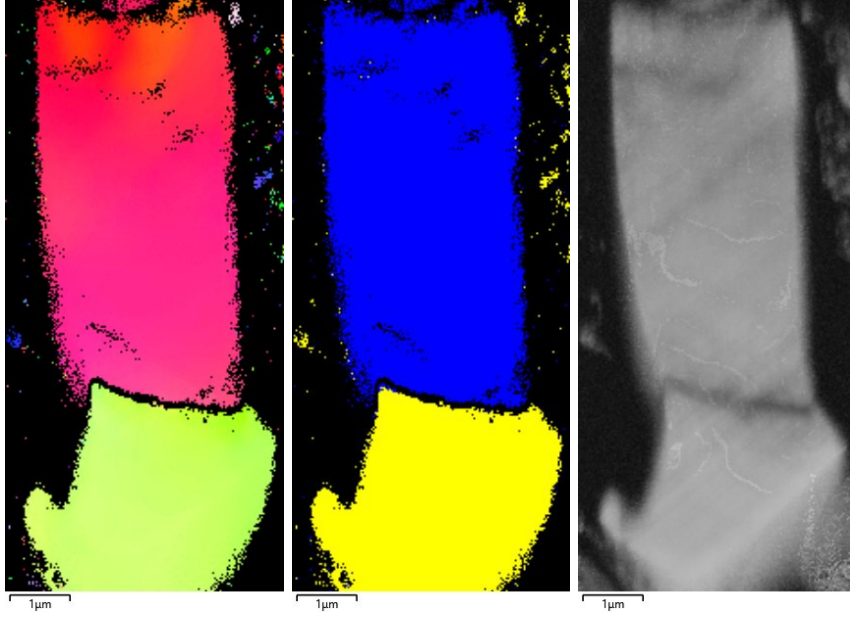
Suppl. Figure S8: **EBSD results**, Sample 1, pillar B6. (left) IPF-Y orientation map. (middle) phase map with colors: FCC – yellow, BCC – blue. (right) Band contrast image.

S3. Poisson's ratio

Two ways of calculating the Poisson's ratio have been considered in this work. The first is to simply average the Poisson's ratio of the constituent elements:

$$\nu_1 = \frac{1}{5} \sum \nu_i = 0.321, \quad i : \mathrm{Ni, Co, Fe, Cr, Ga} \tag{3}$$

with $\nu_{Ni} = 0.31$, $\nu_{Co} = 0.32$, $\nu_{Fe} = 0.293$, $\nu_{Cr} = 0.21$, $\nu_{Ga} = 0.47$. These values were taken from the Goodfellow catalogue of high purity materials [71].

The second method is performed by measuring ultrasonic velocities in the material, and calculating $\nu_2 = 0.294$ by the formula

$$\nu_2 = \frac{v_p^2 - 2v_s^2}{2(v_p^2 - v_s^2)}, \tag{4}$$

where $v_p = 5.22 \times 10^3$ m/s longitudinal and $v_p = 2.82 \times 10^3$ m/s transversal velocities were measured earlier. Eventually, the average of the two calculated values were used in the evaluations of the current work:

$$\bar{\nu} = \frac{1}{2}(\nu_1 + \nu_2) \cong 0.31. \tag{5}$$

The uncertainty of the Poisson's ratio results in ∼1% error in the Young's modulus values.

S4. Micromechanical details
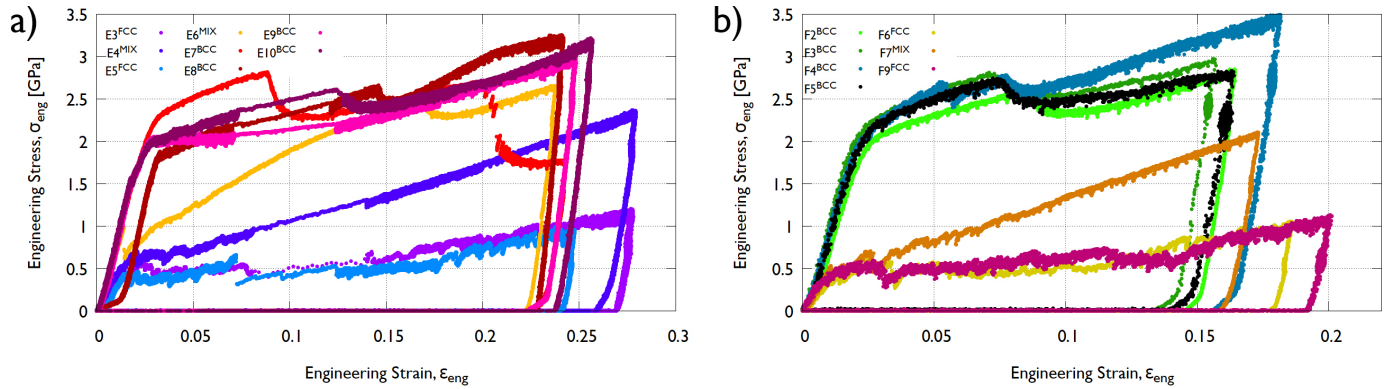
Suppl. Figure S9: **Pillar deformation, series E, F.** Sample 1. Stress-strain curves at quasi-static strain rates. Pillars with (a) 2.5 μm and (b) 1.5 μm diameters. Phase map colors: FCC – yellow, BCC – blue. The $\sigma_{eng} - \varepsilon_{eng}$ curve of pillar "E7" exhibits a slightly different behaviour at the beginning of the loading ($\varepsilon < 0.01$), this is due to the fact that the surface of the pillar was not parallel with the flat punch tip. A unique misalignment like this (when preparing a batch of pillars) is most likely produced by imperfect FIB milling, where a slight beam misalignment would unevenly expose an area, causing the halo of the ion beam to touch only one part of the sample.
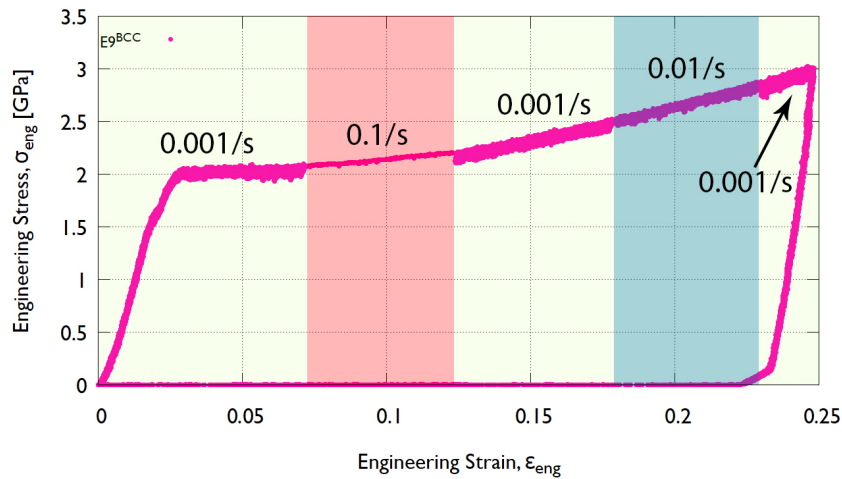
Suppl. Figure S10: **Strain rate jump test**, Sample 1, over the example of the E9 $\sigma_{eng} - \varepsilon_{eng}$ curve.
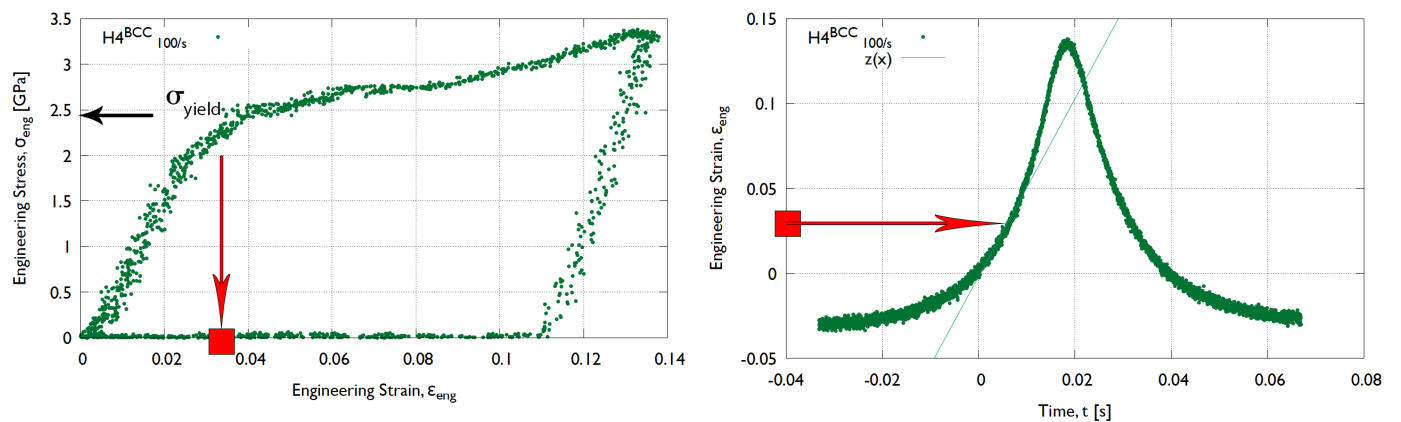
Suppl. Figure S11: **Proportional loading profile.** Sample 1. ε_{eng} variation over time. At the ε_{eng} position related to the σ_{yield}, a "z(x)" linear fit was performed to determine the strain rate upon yielding.
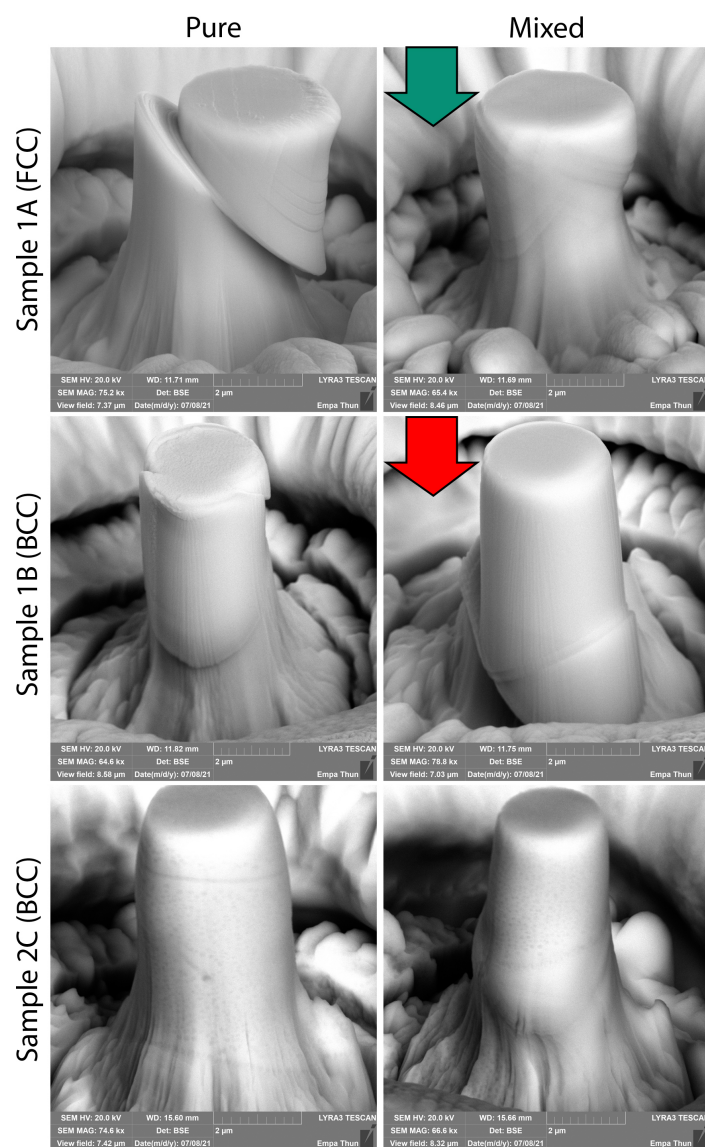
Suppl. Figure S12: **Deformation modes** BSE images
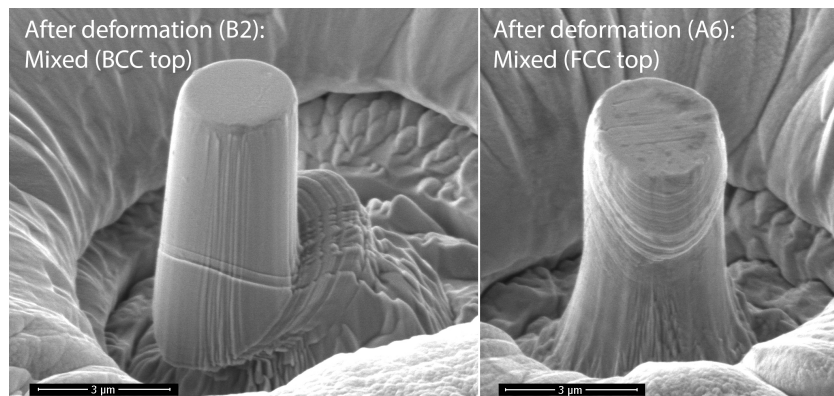
Suppl. Figure S13: **Mixed deformation modes**, Sample 1, SE images.

S5. *Post mortem* microstructure characterization

Suppl. Figure S14: **TOF-SIMS** results along a BCC grain boundary, Sample 2. SE image (in greyscale) highlights the grain boundary between the brighter/darker regions. Many precipitates align with the grain boundary. Coloured images show distributions of the marked ions. Color scales are in arbitrary units (counts/TOF extraction).

Suppl. Figure S15: **TEM imaging** pillar C1, Sample 2 at the BCC (containing precipitates) and FCC interface.

QSSR (0.01/s): pillar K3   UHSR (3900/s): pillar K15   High dislocation density

Suppl. Figure S16: **TEM imaging** Sample 1, pillars at various strain rates. Grain boundaries are marked with dotted white lines.
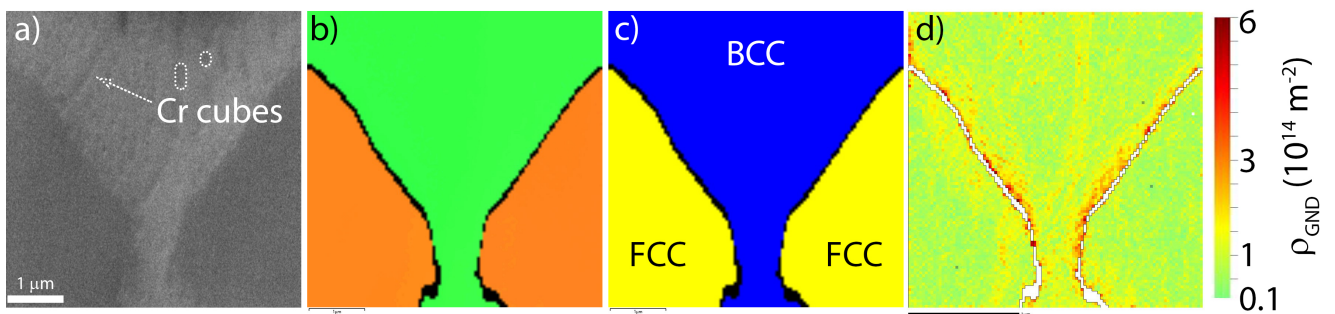
Suppl. Figure S17: **HR-EBSD**, Sample 2, undeformed specimen. (a) Band contrast image of the mapped area. A few precipitates are highlighted with white dashed shapes. (b) IPFz orientation map. (c) Phase contrast map. (d) Map of the estimated GND-density.
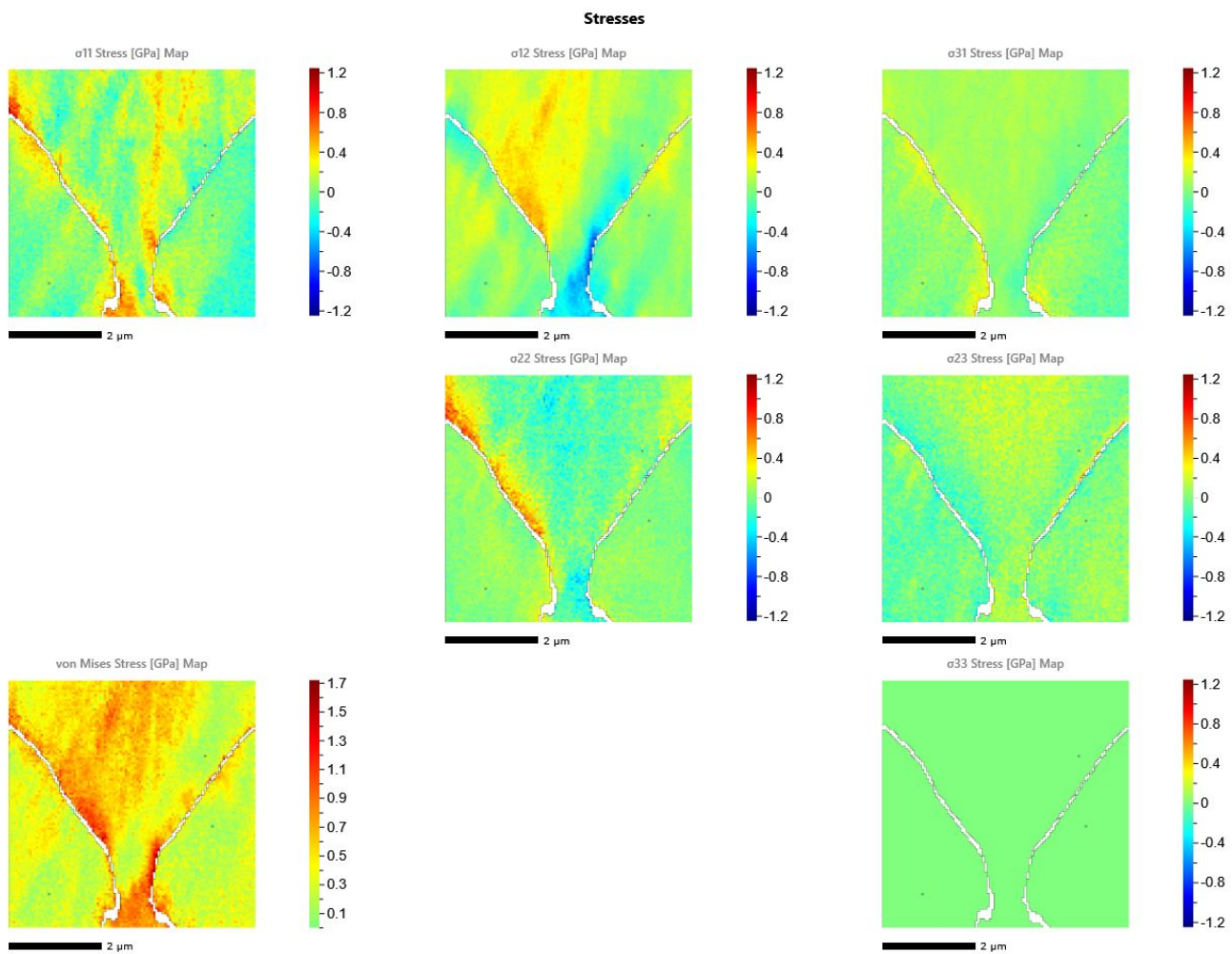
Suppl. Figure S18: **HR-EBSD stress tensor components (σ_{ij}) and von Mises stress**. Sample 2, undeformed specimen.
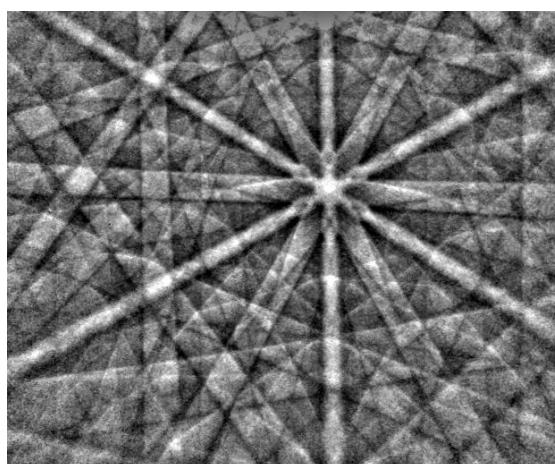
Suppl. Figure S19: **Typical EBSD pattern**, Sample 2.
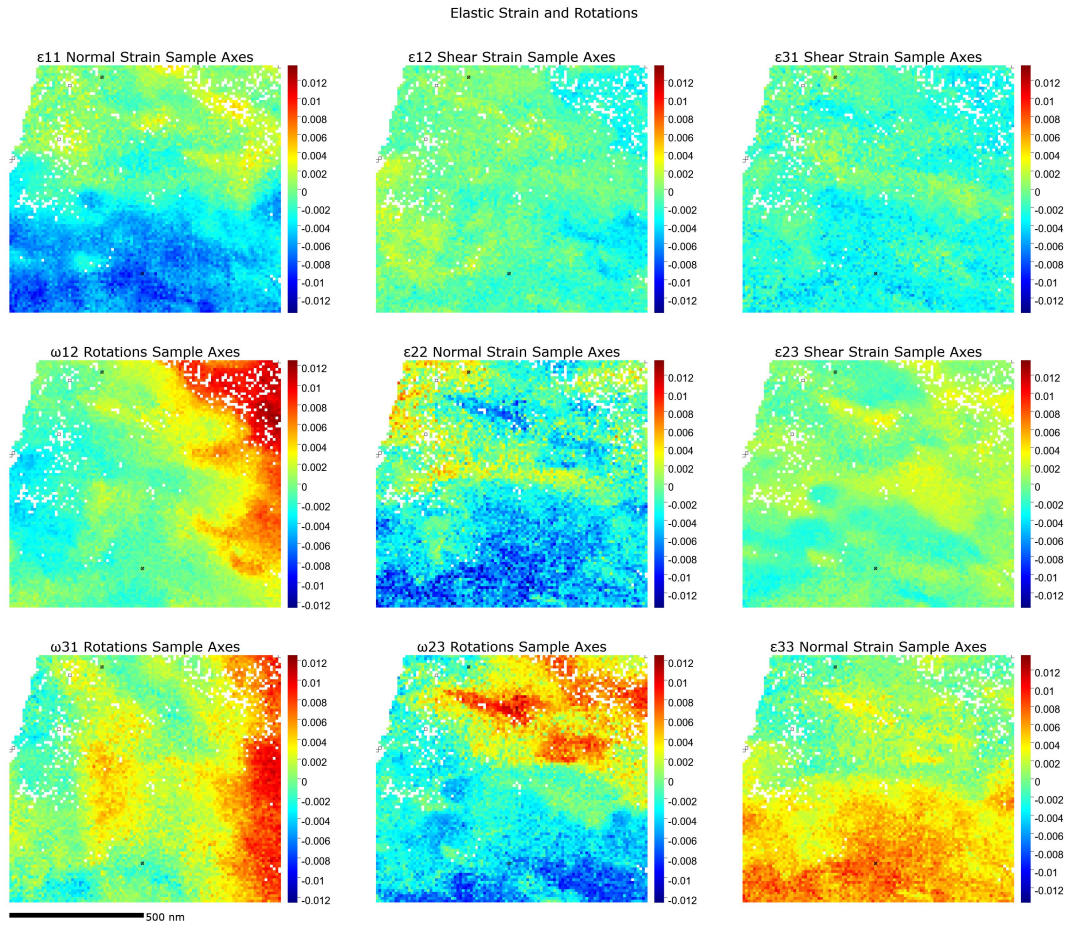
Suppl. Figure S20: **HR-TKD**, C1 strain- and rotation tensor elements, BCC phase.
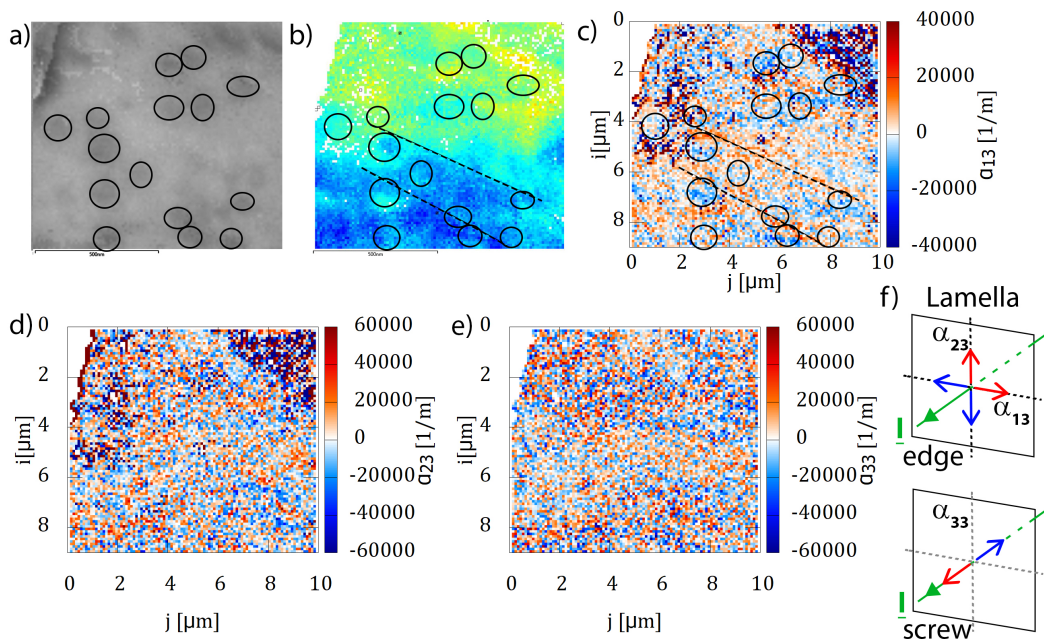
Suppl. Figure S21: **HR-TKD**, C1 Burgers vector analysis on the BCC region. a) Band contrast image, b) ε_{11} map (colors identical to Fig. S20) and c) α_{13} map comparison. Black circles indicate the presence of precipitates, dotted lines show edge type GND density features similar to Fig. 5. d) α_{23} and e) α_{33} maps. f) Sketch indicating the typical Burgers vector directions based on the component analysis.

S6. Pillars' Summary

Pillar name	ID	Phase	Avg. diam. [μm]	Avg. height [μm]	Height (TC) [μm]	Def. mode	Max. def. (%)	Tip v [nm/s]	SR [/s]	Yield stress [MPa]	Smp [Hz]	Load cell	Notes
A1	S1	FCC	3.31	5.28	6.45	pure	23	8	0.001	273	40	SLC-1	
A2			3.39	5.16	6.30	pure	17		0.001	197	40		
A3			3.26	5.52	6.74	mixed	16		0.001	156	40		LO/TEM
A4			3.33	5.64	6.89	pure	17		0.001	196	40		
A5			3.35	6.32	7.72	pure	16		0.001	211	40		
A6			3.33	5.28	6.45	mixed	17		0.001	166	40		
B1	S1	BCC	3.15	5.91	7.21	mixed	17	8	0.001	876	40	SLC-1	
B2			3.14	5.91	7.21	mixed	17		0.001	982	40		
B3			3.22	5.72	6.98	mixed	17		0.001	857	40		LO/HR-EBSD
B4			3.42	6.08	7.42	mixed	17		0.001	643	40		
B5			3.29	6	7.32	pure	17		0.001	1828	40		
B6			3.27	5.88	7.18	pure	15		0.001	1845	40		LO/HR-EBSD
C1	S2	BCC	3.22	5.44	6.64	pure	16	8	0.001	1035	40	SLC-1	LO/TEM
C2			3.31	5.81	7.09	pure	17		0.001	940	40		
C3			3.41	5.85	7.14	pure	17		0.001	954	40		
C4			3.37	6.01	7.34	pure	16		0.001	1076	40		
C5			3.41	6.05	7.39	pure	16		0.001	393	40		
C6			3.36	6.09	7.43	mixed	17		0.001	811	40		
C7			3.25	6.05	7.39	mixed	17		0.001	729	40		
E1	S1	FCC	2.38	3.11	3.95	-	-	5.0	0.001	182	40	MLC-1	side wall touch
E2			2.39	2.96	3.76	-	-	5.0	0.001	233	40		
E3			2.38	3.15	4.00	pure	27	5, 500, 50	SRJT	322	40		
E4			2.35	3.11	3.95	mixed	27	5, 500, 50	SRJT	429	400		
E5			2.36	3.54	4.49	pure	25	5, 500, 50	SRJT	433	400		
E6	S1	BCC	2.45	3.64	4.62	mixed	24	5.0	0.001	1060	40	MLC-1	
E7			2.43	3.57	4.53	pure	24	5.0	0.001	2375	40		
E8			2.41	3.59	4.56	pure	26	5, 500, 50	SRJT	1886	400		
E9			2.39	3.49	4.43	pure	25	5, 500, 50	SRJT	1616	400		
E10			2.38	3.36	4.26	pure	26	5, 500, 50	SRJT	1553	400		

Suppl. Table S2: Pillar parameters. Avg.: average, TC: tilt corrected, v: velocity, Smp: sampling rate, SRJT: strain rate jump test, LO: lift-out. **Bold font** indicates the samples used for the SRS plot in Fig. 4, *italic font* represents the pillars selected for Fig. 3.

Pillar name	ID	Phase	Avg. diam. [μm]	Avg. height [μm]	Height (TC) [μm]	Def. mode	Max. def. (%)	Tip v [nm/s]	SR [/s]	Yield stress [MPa]	Smp [Hz]	Load cell	Notes
F1	S1	BCC	1.53	2.31	2.93	mixed	-	3.5	0.001	1268	40	MLC-1	side wall touch
F2			1.53	2.32	2.94	pure	16	3.5	0.001	1987	40		
F3			1.48	2.39	3.03	pure	16	350	0.1	2177	400		
F4			1.48	2.06	2.61	pure	17	35	0.01	1988	400		
F5			1.48	2.3	2.92	pure	16	350	0.1	2037	1000		
F6	S1	FCC	1.43	2.06	2.61	pure	18	3.5	0.001	359	40	MLC-1	
F7			1.41	2.2	2.79	mixed	17	3.5	0.001	528	40		
F8			1.44	1.99	2.53	-	-	350	0.1	468.2	400		
F9			1.42	1.87	2.37	pure	20	35	0.01	383	400		
F10			1.43	1.6	2.03	-	-	350	0.1	443	1000		
G1	S1	FCC	-	-	-	-	-	-	-	-	-		no data
G2			1.46	3.37	4.28	pure	14	prop.	12	866.7	100k	ST	
G3			1.56	3.65	4.63	pure	12	prop.	6	520.1	50k		
G4			1.53	3.37	4.28	pure	9	prop.	2	619.5	50k		
G5			1.53	3.58	4.54	pure	30	prop.	2	489.8	50k		
G6			2.55	3.19	4.05	mixed	21	prop.	16	561.8	100k		
G7			2.93	3.97	5.04	pure	16	prop.	6	350.6	100k		
G8			2.55	3.26	4.14	pure	21	prop.	2	479	50k		
G9			2.53	3.24	4.11	pure	21	prop.	1	592	50k		
G10			2.56	3.41	4.33	mixed	19	prop.	16	618.4	100k		
H1	S1	BCC	2.56	3.76	4.77	mixed	16	prop.	9	1220	100k	ST	
H2			2.55	3.6	4.57	mixed	18	prop.	6	1180	100k		
H3			2.63	4.04	5.13	mixed	17	prop.	2	897.8	50k		
H4			2.63	4.05	5.14	pure	14	prop.	5	2274	50k		
H5			2.7	4.15	5.27	pure	12	prop.	60	2064	100k		
H6			1.48	2.36	2.99	pure	21	prop.	25	2742	100k		
H7			1.46	1.62	2.06	pure	32	prop.	27	2557	100k		
H8			1.59	2.49	3.16	pure	20/25	prop.	7	2182	50k		
H9			1.58	2.64	3.35	pure	20/25	prop.	2	2191	50k		
H10			1.61	2.64	3.35	pure	17	prop.	24	2085	100k		
I1	S1	FCC	2.37	3.7	4.70	-	-	6×10^6	1278	-	1M	ST	ringing
I2			2.44	3.64	4.62	-	-	5.9×10^6	1277	-	500k		ringing
I3			2.48	3.91	4.96	-	-	5.9×10^6	1189	-	500k		ringing
I4			2.46	3.59	4.56	-	-	6.0×10^6	1317	732	500k		
I5			2.47	3.28	4.16	-	-	6.0×10^6	1442	607	500k		
I6			1.51	3.13	3.97	-	-	10×10^6	2518	661	500k		ringing
I7			1.56	2.92	3.71	-	-	0.5×10^6	135	475	50k		
I8			1.52	2.88	3.65	-	-	6.0×10^6	1642	-	500k		ringing
I9			1.56	3.75	4.76	-	-	6.0×10^6	1261	-	500k		ringing
I10			1.43	3.09	3.92	-	-	6.0×10^6	1530	-	500k		ringing

Suppl. Table S3: Pillar parameters. Avg.: average, TC: tilt corrected, v: velocity, Smp: sampling rate, ST: SmarTip piezo based load cell, prop.: proportional loading profile. **Bold font** indicates the samples used for the SRS plot in Fig. 4, *italic font* represents the pillars selected for Fig. 3.

Pillar name	ID	Phase	Avg. diam. [μm]	Avg. height [μm]	Height (TC) [μm]	Def. mode	Max. def. (%)	Tip v [mm/s]	SR [/s]	Yield stress [MPa]	Smp [Hz]	Load cell	Notes
J1	S1	BCC	2.44	4.05	5.14	-	-	6.0	1167	2435	200k	ST	
J2			2.48	4.32	5.48	-	-	6.0	1094	2206	200k		
J3			2.43	4.02	5.10	-	-	6.0	1176	2575	500k		
J4			2.39	3.99	5.06	-	-	6.0	1185	1050	500k		
J5			2.48	4.09	5.19	-	-	0.66	127	1111	25k		
J6			1.48	3.27	4.15	-	-	6.0	1446	2859	500k		
J7			1.53	2.77	3.52	-	-	6.0	1707	-	500k		
J8-J10			-	-	-	-	-	-	-		-		destroyed
J11			1.55	2.65	3.36	-	-	6.0	1784	2642	500k		
K1	S1	BCC	2.56	2.81	3.43	-	-	30	8746	3961	1M	ST	
K2			2.46	2.57	3.14	-	-	30	9562	4740	1M	ST	
K3			2.52	2.75	3.36	pure	-	30	0.01	1793	40	SLC	LO/TEM
K4			2.41	2.59	3.16	-	-	30	9488	-	1M	ST	no def., LO/TEM
K5			2.38	2	2.44	mixed	-	3×10^{-5}	0.01	848.2	40	SLC	
K6			2.4	2.49	3.04	-	-	3×10^{-5}	0.01	2214	40	SLC	LO/TEM
K7		FCC?	2.35	2.29	2.80	mixed	-	10	3577	661	500k	ST	pancake
K8			1.63	2.56	3.13	-	-	10	3200	2618	500k	ST	pancake
K9			1.58	2.38	2.91	-	-	10	3442	2740	500k	ST	pancake
K10			1.59	2.34	2.86	-	-	10	3501	3033	500k	ST	pancake
K11		FCC?	1.54	2.11	2.58	mixed	-	30	11647	1420	1M	EST	
K12			1.58	2.53	3.09	-	-	30	9713	5600	1M	EST	
K13			1.53	2.35	2.87	-	-	50	17429	6700	1M	EST	
K14			1.52	1.98	2.42	-	-	10	4137	2580	1M	EST	
K15			1.52	2.1	2.56	-	-	10	3901	3330	1M	EST	LO/TEM
M1	S1	FCC	1.47	3.11	3.95	-	-	10	2534	918	1M	ST	
M2			1.43	3.14	3.98	-	-	10	2510	822			
M3			1.45	3.54	4.49	-	-	30	6678	1260			
M4			1.49	3.34	4.24	-	-	30	7078	1169			
M5			1.52	3.58	4.54	-	-	50	11006	-			destroyed
M6			1.46	3.49	4.43	-	-	50	11290	1074			
M7			1.49	3.4	4.31	-	-	50	11589	1180			
M8			1.44	2.9	3.68	-	-	30	8152	1250			
M9			1.46	3.33	4.23	-	-	50	11832	1106			
M10			1.43	3.37	4.28	-	-	50	11692	1000			

Suppl. Table S4: Pillar parameters. Avg.: average, TC: tilt corrected, v: velocity, Smp: sampling rate, ST: SmarTip piezo based load cell, EST: Enhanced SmarTip, LO: lift-out. **Bold font** indicates the samples used for the SRS plot in Fig. 4.